Journal of Elasticity (2022) 155:393–423
https://doi.org/10.1007/s10659-022-09962-9

# Stability and Localization of Deformation Delay in Finitely Strained Plates at Arbitrary Strain-Rates

**G. Wen[1] · K. Ravi-Chandar[2] · R.S. Elliott[3] · N. Triantafyllidis[1,4,5]**

Received: 25 July 2022 / Accepted: 2 December 2022 / Published online: 21 December 2022


**Abstract**
Of interest here is the stability and associated deformation localization of structures when inertial effects are considered. Concerned primarily with the study of necking failure patterns, the prevailing approach in the relevant literature uses the "*modal analysis*" method to find the wavelength of the structure's fastest growing eigenmode, an approach that often uses a rate-dependent material response. However, the experimental studies of (Zhang and Ravi-Chandar in Int. J. Fracture 142: 183–217, 2006; Zhang and Ravi-Chandar in Int. J. Fracture 163: 41–65, 2010) on the high strain-rate expansion of thin rings and tubes, show no evidence of a dominant wavelength in their failure mode and no influence of strain-rate sensitivity on the necking strains. Moreover, modal analysis assumes that at all times the entire structure sees the applied eigenmode perturbation in spite of the physical limitation of a finite wave propagation speed. In addition, the closely related problem of stability in dynamically loaded structures, i.e., the time evolution of perturbations introduced at different times during loading, does not seem to have attracted attention.

Based on the above-mentioned experimental and theoretical observations, (Ravi-Chandar and Triantafyllidis in Int. J. Solids Struct. 58: 301–308, 2015) proposed a "*localized perturbation*" approach to study the dynamic stability of an incompressible, nonlinearly elastic bar at different strain-rates by following the evolution of spatially localized small perturbations introduced at different times. The goal of the present work is to study the dynamic stability – linear and nonlinear – of rate-independent biaxially strained thin plates by following the evolution of spatially localized perturbations introduced at different times, to understand the initiation of the corresponding failure mechanisms. Our 2D linearized analysis of a thin plate under plane stress state, shows that these plates are stable until $\tau_L$, the dimensionless limit time corresponding to the loss of the uniformly strained plate's stability. This result is supported by fully nonlinear calculations.

Our nonlinear numerical calculations also show an imperfection amplitude-dependent and biaxiality-dependent delay in the appearance of localization patterns in dynamically loaded plates for dimensionless times well beyond $\tau_m$, corresponding to the onset of loss of ellipticity in the constitutive law. Moreover, the failure patterns of these plates are studied numerically by following the time evolution of randomly distributed imperfections of different amplitudes.

**Keywords** Inertia · Nonlinear elasticity · Elasto-plasticity · FEM methods · Stability · Dynamics

Extended author information available on the last page of the article

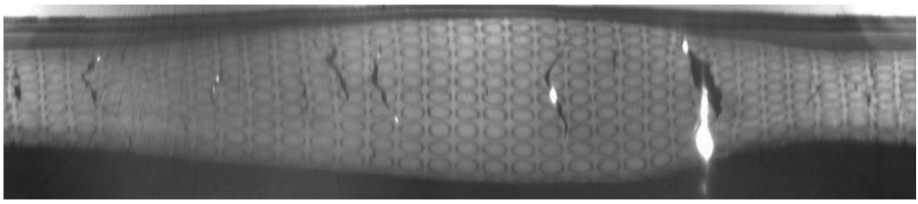

**Fig. 1** Unfolded conical mirror image for an electromagnetically expanding Al 6061-O tube test (from [34]), showing the necks and fractures in the thin cylindrical sheet under high strain rate loading; notice the absence of a dominant wavelength in the failure pattern

**Mathematics Subject Classification (2010)** 74B20 · 74C15 · 74H15 · 74H55 · 74K15

## 1 Introduction

The stability of structures when inertial effects are considered is an important engineering problem and as such has drawn considerable attention. The first investigation in this area appears to be the work of [14] on the influence of inertia in a simply supported imperfect column subjected to a sudden axial load. A substantial amount of work followed that studied the response of, mainly elastic, structures to impulse or time-dependent loads. Due to the many possible definitions for the stability of time-dependent systems, the term "*dynamic stability*" encompasses many classes of problems and different physical phenomena and has numerous interpretations, with inertia being the common denominator.

In the absence of inertia, the processes of failure by a bifurcation instability mode in elastic solids and structures is well understood (e.g., textbook by [3]) and a general asymptotic analysis, termed "*Lyapunov-Schmidt-Koiter*" (LSK), has been developed for their study, independently introduced for structures in the celebrated thesis of W. T. Koiter [13]. The first effort to use the LSK analysis for the dynamic stability problem of an elastic structure appears to be [4], where the authors proposed an asymptotic analysis of the time-dependent problem using the eigenmodes of the static problem.

Motivated primarily by the study of necking failure patterns, an idea popular in fluid mechanics has been adopted for the dynamic linear stability analysis of solids and structures with more general constitutive laws under high rates of loading. It is termed the "*modal analysis*" method and consists of seeking the solid's fastest growing eigenmode and the associated wavelength to determine the strain at onset of necking. This method has been repeatedly applied to the study of dynamic stability of various rate-dependent (elasto-visco-plastic) structures (bars, rings, plates, shells etc.) under rapid loading rates where the failure pattern and size of fragments is of interest. Although there is a vast literature on this topic (for a review see [7]), a short account is provided here to place the present work in the proper context.

Starting in the early 1980's, the dynamic localization of deformation problem – called a "*band*" for shearing, and "*necking*" for uniaxial tension – was investigated in a series of papers: [5, 8, 9, 17], using the frozen coefficient linearized stability approach; this work showed that inertia, triaxiality and viscosity play a significant role in the development of dynamic localization phenomena. Specifically, it was demonstrated that inertia decreased the growth rate of long wavelength perturbations while triaxiality and viscosity inhibited growth rate of short wavelength perturbations. Several other studies have also followed along these lines: [10, 11, 23, 30, 35], examining axisymmetric rods and 2D plane strain conditions, with

similar conclusions. Necking under biaxial strain states (2D) has also been examined (e.g., [12, 16]) using the same linearized stability analysis framework concluding, once again, that inertia restricts growth of long wavelength modes while multidimensionality is sufficient to limit short wavelengths. While the modal analysis approach identifies – with the help of viscous effects – the fastest growing eigenmode, it lacks predictive capability in identifying the strain at onset of necking; [10] suggested choosing a critical value of the ratio of the perturbation growth rate to the background strain rate to fit the experimental data on neck spacing, but there appears to be no guiding principle for this selection.

The linear perturbation modal analyses have been augmented with various features through analytical models and numerical simulations that incorporated defects through different idealizations. For example, [35] performed detailed numerical simulations of fragmentation in a uranium-6%-niobium (U6N) ring introducing numerous defects in the initial cross sectional area to trigger localization; the resulting simulated fragment distribution was shown to agree well with experimental observations. [6] considered fragmentation of a uniformly stretching rod using a modified Mott approach. In this approach, the fastest growing perturbation modes were first identified through a linearized stability analysis; then statistics of fragmentation was investigated by considering a distribution of potential failure sites governed by the mode derived from the linear stability analysis. Both single mode perturbation with a random strain to failure and a multimode perturbation with a constant strain to failure were considered. Subsequent work by [21, 22, 27, 28, 31] augmented perturbation analyses with detailed finite element simulations to provide an evaluation of the necking patterns formed, influenced by defects, inertia, constitutive model and other aspects. Although the interest of the present work focuses on the initiation of necking failure patterns, it should also be mentioned here that fracture plays an important role in understanding the dynamic failure patterns (e.g., see [18] and references quoted therein).

The overall outcome of the modal approach for the study of failure patterns in rapidly loaded solids and structures may be summarized as follows: for the rate-independent case, modes become unstable beyond a critical strain level, with all wavelengths indicating such instability and therefore not selecting a wavelength as is typical of linearized stability analysis in the static loading of structures case. Consequently, constitutive rate effects (viscoelasticity) are indispensable for determining the eigenmodes' growth rate, which is dependent on the wavelength. The wavelength corresponding to the maximum growth rate for perturbations is then selected as the wavelength of necking, but this identification depends on imposing a criterion of critical growth rate; given such a selection criterion, the strain at onset of necking shows an increase from the corresponding static necking strain, the Considère strain in 1D or the loss of ellipticity strain in 2D and 3D; this has been called the "*dynamic delay*". These observations apply generally to problems of axisymmetric, plane-strain and 3D conditions. Still there exist open questions related to the critical strain at onset of necking/localization, spacing and pattern formation, role of defects and statistical aspects, etc.

However, experiments from rapidly expanding, electromagnetically loaded metallic rings and tubes by [32–34] show no dominant wavelength of the necked pattern, as seen in the onset of failure of an electromagnetically loaded, dynamically expanding tube depicted in Fig. 1, where one can observe a rather random failure mode. Moreover, they find no evidence of viscoplastic response, i.e., no influence of strain rate on the necking strains,[1] results in agreement to the maximum force criterion of a rate-independent constitutive law (Considère criterion). As explained by these authors, using the fastest growing eigenmode to predict

[1] Strain rates investigated were of order up to $10^4\,\mathrm{sec}^{-1}$.

the onset of failure is physically meaningful provided that some characteristic velocity of the principal solution – e.g., ring/tube expansion rate – is much slower than the speed of propagation of perturbations in the solid or structure at hand. In addition, the closely related problem of stability in dynamically loaded structures, i.e., the time evolution of perturbations introduced at different times during loading, does not seem to have attracted attention.

Motivated by the above observations, [20] studied the dynamic stability of an incompressible, nonlinearly elastic bar at different strain rates using a novel approach, termed "*localized perturbation*" approach, which involves the study of evolution of spatially localized perturbations introduced at different times. The same approach is adopted here for the dynamic stability of biaxially strained thin plates, following the work of [29], who defined the concept of influence discs and followed, using numerical (FEM) calculations, the dynamic evolution of initial imperfections in the context of rate-independent elastoplastic constitutive laws. The goal of the present work is to apply the spatially localized perturbation approach to study the dynamic stability and associated localization of deformation (necking) delay of a biaxially loaded thin plate under plane stress conditions, both theoretically using a linearized method and full numerical calculations.

The presentation is organized as follows: after the introduction in Sect. 1, the linearized and nonlinear perturbation problems are presented in Sect. 2. A dimensionless form of the governing equations is introduced together with the "*loading rate parameter*" $\eta$ that relates the mechanical loading rate (transverse strain-rate) to the axial wave propagation speed at zero strain. Our general frozen-coefficient linearized stability analysis shows that the plate is stable for perturbations at times below $\tau_L$, the dimensionless time limit corresponding to the loss of the uniformly strained plate's linearized stability (which is independent of $\eta$). We establish that $\tau_L \leq \tau_m$, the latter defined as the dimensionless time for onset of loss of ellipticity in the constitutive law. We also find that the plate has always the possibility to experience an immediate growth of some perturbation.[2] Results are given in Sect. 3, starting with the fully nonlinear (numerical) stability analysis – for mechanical loading rates commensurate to the wave propagation speed ($\eta = 1$) – that confirms the findings of its linearized counterpart and clearly show an imperfection amplitude-dependent and biaxiality-dependent delay in the localization of deformation of the rapidly strained, locally perturbed, plate as opposed to its statically loaded counterpart. We proceed next with the time evolution of an initial defect and continue by studying the effect of unloading, which becomes important well after the critical time $\tau_m$. We end with the nonlinear time evolution of randomly distributed localized initial imperfections of different amplitudes, in order to explain the deformation pattern mechanism for the rapidly strained plate, elastic as well as elastoplastic (both with the same uniaxial response). Conclusions are presented in Sect. 4. Details on the different constitutive laws and their incremental moduli used in the linearized analyses are presented in Appendix A, the corresponding influence discs are presented in Appendix B and the dimensionless "*critical time*" ($\tau_m$) and "*stability limit*" time ($\tau_L$) used for the calculations of Sect. 3 are recorded in Appendix C.

## 2 Stability Analysis

This section starts with the presentation of the 2D model for the dynamic loading a biaxially strained, rate-independent, flat plate of infinite extent and provides the problem's dimensionless critical time $\tau_m$. The frozen coefficient linearized stability of a spatially localized

[2] Plate is unstable under the "*transient growth criterion*" used in fluid mechanics, e.g., see [25].

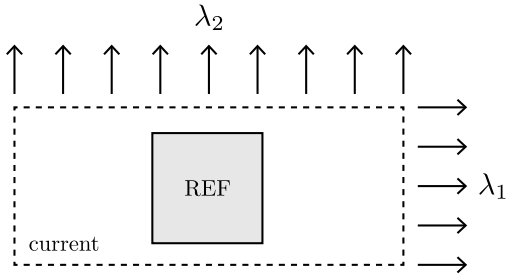


**Fig. 2** A schematic diagram of a biaxially strained plate subjected to stretch ratios $\lambda_1, \lambda_2$

perturbation is considered next, showing that if the plate is perturbed at a (dimensionless) time inferior to the stability limit time $\tau_L$, then this perturbation's amplitude will decay. The concept of the initial response of the perturbation (transient growth) is also investigated followed by a brief description of the numerical (FEM) solution for the corresponding fully nonlinear problem.

### 2.1 Problem Setting

Although a detailed version of the problem setting and the introduction of the dimensionless critical time $\tau_m$ and critical length $\delta_-$ has been presented in [29], a brief description is given here in the interest of completeness. We consider a two-dimensional thin, flat plate (idealized as a membrane) of infinite extent and uniform initial thickness $H$ subjected to a biaxial straining as shown in Fig. 2. To avoid in-plane acceleration terms in the unperturbed solution of the perfect plate, a uniform deformation with stretch ratios[3] $\lambda_\alpha$ and straining rate $c$ is imposed at time $t$

$$\lambda_1 = 1 + ct\cos\psi\ , \quad \lambda_2 = 1 + ct\sin\psi\ . \tag{2.1}$$

In the absence of body forces, the equations of motion for the thin plate can be put in the form

$$\frac{\partial N_{\alpha\beta}}{\partial X_\beta} = \rho_0 \frac{\partial v_\alpha}{\partial t}\ , \tag{2.2}$$

where $N_{\alpha\beta}$ are the components of the nominal (force/reference thickness) membrane stress resultant $\mathbf{N}$, $\rho_0$ the reference mass density,[4] $X_\alpha$ the reference geometric coordinates and $v_\alpha(\mathbf{X}, t)$ the components of the velocity $\mathbf{v}$ of a material point initially at $\mathbf{X}$. A Lagrangian formulation is adopted here and the reference configuration is identified with the stress-free configuration of the plate.

From kinematics, we have a compatibility relation between the rate[5] of deformation gradient $\dot{\mathbf{F}}$ and the gradient of material point velocity $\mathbf{v}$

$$\frac{\partial F_{\alpha\beta}}{\partial t} = \frac{\partial v_\alpha}{\partial X_\beta}\ . \tag{2.3}$$

[3] Henceforth, Greek indexes range from 1 to 2 while Latin indexes range from 1 to 3.

[4] The reference mass density $\rho_0$ is per unit reference area.

[5] Henceforth a superimposed dot denotes time differentiation at a fixed material point initially at $\mathbf{X}$, i.e., $\dot{f} \equiv \partial f(\mathbf{X}, t)/\partial t$.

To complete the nonlinear system of (2.2) and (2.3), a constitutive law for the plate is needed, relating $\mathbf{N}$ to $\mathbf{F}$. For a hyperelastic solid, the membrane stress components are derivable from a potential

$$N_{\alpha\beta} = \frac{\partial W}{\partial F_{\alpha\beta}} , \tag{2.4}$$

where $W(\mathbf{F})$ is the two-dimensional strain energy density of the plate. For the more general case of a rate-independent material, the constitutive law can be expressed by the following relation between the time derivative of the stress measure $\dot{\mathbf{N}}$ and its work-conjugate rate of deformation gradient $\dot{\mathbf{F}}$, namely

$$\dot{N}_{\alpha\beta} = \mathcal{L}_{\alpha\beta\gamma\delta}\dot{F}_{\gamma\delta} , \tag{2.5}$$

where $\mathcal{L}_{\alpha\beta\gamma\delta}$ are the plane stress incremental moduli of the plate. These moduli depend in general on the current state of stress and the deformation history, typically represented by a set of internal variables. They are obtained from the three-dimensional version of the constitutive law $\dot{\Pi}_{ij} = L_{ijkl}\dot{F}_{kl}$ (relating the rate of the nominal stress tensor $\dot{\mathbf{\Pi}}$ to its work-conjugate quantity $\dot{\mathbf{F}}$) plus the plane stress condition $\dot{\Pi}_{i3} = 0$ and the orthotropy of the plate with respect to the thickness direction (see Appendix A). For the case of a hyperelastic material, the components of the plane stress incremental moduli tensor are obtained from (2.4) and (2.5) by

$$\mathcal{L}_{\alpha\beta\gamma\delta} = \frac{\partial^2 W}{\partial F_{\alpha\beta}\partial F_{\gamma\delta}} . \tag{2.6}$$

It can be shown, e.g., [29], that the square of wave propagation speed $V$ along a direction $\mathbf{n}$ (polarization vector) is one of the two eigenvalues of the acoustic tensor $\mathbf{A}(\mathbf{n})$

$$\left[A_{\alpha\gamma}(\mathbf{n}) - \rho_0(V)^2\delta_{\alpha\gamma}\right]C_\gamma = 0 , \quad A_{\alpha\gamma}(\mathbf{n}) \equiv \mathcal{L}_{\alpha\beta\gamma\delta}n_\beta n_\delta . \tag{2.7}$$

To deal with dimensionless quantities we define a dimensionless space variable ($\boldsymbol{\chi}$), a dimensionless time ($\tau$) and a dimensionless energy density ($\mathcal{W}$)

$$\boldsymbol{\chi} \equiv \mathbf{X}/H , \quad \tau \equiv ct , \quad \mathcal{W} \equiv W/EH . \tag{2.8}$$

We also introduce the dimensionless "*loading rate parameter*" ($\eta$) that relates the mechanical loading rate (transverse strain-rate) $cH$ to the speed of wave propagation $\sqrt{[EH/\rho_0]}$, the one-dimensional wave propagation speed in a stress-free bar made of the same material as the plate ($E$ being the corresponding Young's modulus of the solid). For $\eta \ll 1$ we approach static loading rates while for $\eta = 1$ (the value taken for all subsequent numerical calculations) the mechanical loading rate is commensurate to the axial wave propagation speed.

$$\eta \equiv cH\,[EH/\rho_0]^{-1/2} . \tag{2.9}$$

Some additional dimensionless characteristic lengths, $\delta_-$ and $\delta_+$, play an important role for this problem and are defined as follows. We consider the lowest dimensionless wave propagation speed $v_-$ which is the lowest eigenvalue of the acoustic tensor defined in (2.7)

appropriately non-dimensionalized with the help of (2.8). The perturbation can no longer propagate along a direction $\phi$ once its lowest speed reaches $v_- = 0$, occurring at time $\tau_e(\phi)$

$$v_-(\phi, \tau_e(\phi)) = 0\,; \quad (v_-(\phi, \tau) > 0 \text{ for } 0 \le \tau < \tau_e(\phi)) \ . \tag{2.10}$$

The problem's dimensionless "*critical time*" $\tau_m$, is the lowest value of $\tau_e(\phi)$, for $\phi \in [0, \pi)$[6] occurring at angle $\phi_m$

$$\tau_m = \min_{\phi\in[0,\pi)} \tau_e(\phi) = \tau_e(\phi_m) \ . \tag{2.11}$$

At time $\tau_m$ the plate reaches for the first time conditions of loss of ellipticity of its incremental equilibrium equations. The corresponding characteristic dimensionless length $\delta_-$ is the radius of the maximum disc entirely influenced by the perturbation at $\boldsymbol{\chi} = \mathbf{0}$ at the onset of loss of ellipticity[7]

$$\delta_- \equiv \min_{\phi\in[0,\pi)} \int_0^{\tau_m} v_-(\phi, \tau)\, \mathrm{d}\tau \ . \tag{2.12}$$

In a similar way we are interested in the maximum size disc, centered at $\boldsymbol{\chi} = \mathbf{0}$, beyond which the plate remains entirely unperturbed at time $\tau_m$, and in analogy to $\delta_-$, we can define $\delta_+$ by

$$\delta_+ \equiv \max_{\phi\in[0,\pi)} \int_0^{\tau_m} v_+(\phi, \tau)\, \mathrm{d}\tau \ , \tag{2.13}$$

where $v_+$ is the larger dimensionless eigenvalue of the acoustic tensor.

It should be noted here that $\delta_-$ and $\delta_+$ exist as long as the model loses ellipticity for some loading. These quantities are useful when selecting domain sizes in the ensuing numerical calculations, where the chosen domain contains a disc larger than a disc of radius $\delta_+$ to ensure that no perturbation reaches the boundary at least up to the time of interest.

### 2.2 Linearized Stability

In order to obtain an analytically tractable way to investigate the stability of the plate's uniform strain solution (2.1), we study the response of the system (2.2)–(2.5) to follow the evolution of a spatially localized perturbation, using the non-dimensionalization[8] of the problem introduced in (2.8). Defining the displacement and particle velocity perturbations[9]

$$\begin{aligned} \delta u_\alpha(\boldsymbol{\chi}, \tau) &\equiv u_\alpha(\boldsymbol{\chi}, \tau) - u^0_\alpha(\boldsymbol{\chi}, \tau)\,; \quad u^0_1(\boldsymbol{\chi}, \tau) = \tau\, \chi_1 \cos(\psi)\,, \quad u^0_2(\boldsymbol{\chi}, \tau) = \tau\, \chi_2 \sin(\psi)\,, \\ \delta v_\alpha(\boldsymbol{\chi}, \tau) &\equiv v_\alpha(\boldsymbol{\chi}, \tau) - v^0_\alpha(\boldsymbol{\chi})\,; \quad v^0_1(\boldsymbol{\chi}) = \chi_1 \cos(\psi)\,, \qquad v^0_2(\boldsymbol{\chi}) = \chi_2 \sin(\psi)\,, \end{aligned} \tag{2.14}$$

[6] From symmetry considerations $A_{\alpha\gamma}(\mathbf{n}) = A_{\alpha\gamma}(-\mathbf{n})$.

[7] In the problem investigated here we also have $\delta_- = \int_0^{\tau_m} v_-(\phi_m, \tau)\, \mathrm{d}\tau$.

[8] Hereinafter, for simplicity the same symbols, $u$ and $v$, are used for the dimensionless quantities as for their dimensioned counterparts while a superimposed dot denotes differentiation with respect to $\tau$.

[9] Hereinafter a superscript $(^0)$ or subscript $(_0)$ denotes evaluation of a quantity on the uniform strain principal solution.

and considering the rate of the equation of motion (2.2) in dimensionless form, one obtains upon linearization about the uniform strain solution

$$\frac{\partial \mathcal{L}_{\alpha\beta\epsilon\zeta}}{\partial F_{\gamma\delta}}\bigg|_0 \dot{F}^0_{\epsilon\zeta} \frac{\partial^2 \delta u_\gamma}{\partial \chi_\delta \partial \chi_\beta} + \mathcal{L}^0_{\alpha\beta\gamma\delta} \frac{\partial^2 \delta v_\gamma}{\partial \chi_\delta \partial \chi_\beta} = \eta^2 \delta \ddot{v}_\alpha \,. \tag{2.15}$$

From the perturbation in the constitutive relation in (2.5) evaluated on the principal solution one has

$$\mathcal{L}^0_{\alpha\beta\gamma\delta} \frac{\partial^2 \delta u_\gamma}{\partial \chi_\delta \partial \chi_\beta} = \eta^2 \delta \dot{v}_\alpha \,. \tag{2.16}$$

The above system (2.15) and (2.16) together with the initial conditions $\delta u_\alpha(\boldsymbol{\chi}, \tau_0)$ and $\delta v_\alpha(\boldsymbol{\chi}, \tau_0)$, i.e., the initial displacement and velocity perturbations, gives the evolution of a perturbation introduced at time $\tau_0$ into the perfect plate deforming in a state of uniform, biaxial strain as described by (2.1). This system of partial differential equations has spatially constant but time-dependent coefficients, which render the finding of a general solution a formidable task. Of interest here is the establishment of the "*frozen-coefficient linearized stability*" of such a perturbation – hereinafter for simplicity referred to as "*linearized stability*" – that requires investigation of this system for time-independent coefficients, evaluated at $\tau_0$. The resulting system is solved with the help of the Fourier transform, in view of the infinite spatial domain of the plate, i.e., $\boldsymbol{\chi} \in \mathbb{R}^2$.

Since spatially localized perturbations (of adequate regularity) are of interest, they have a compact support and hence they admit a Fourier transform, where $\boldsymbol{\chi} \longrightarrow \boldsymbol{\omega}$. Denoting the Fourier transform of $\delta\mathbf{u}(\boldsymbol{\chi}, \tau)$ and $\delta\mathbf{v}(\boldsymbol{\chi}, \tau)$ by $\Delta\mathbf{u}(\boldsymbol{\omega}, \tau)$ and $\Delta\mathbf{v}(\boldsymbol{\omega}, \tau)$ respectively, one obtains from the Fourier transform of (2.15) and (2.16)

$$-\omega_\delta \omega_\beta \left( \frac{\partial \mathcal{L}_{\alpha\beta\epsilon\zeta}}{\partial F_{\gamma\delta}}\bigg|_0 \dot{F}^0_{\epsilon\zeta} \right) \Delta u_\gamma - \omega_\delta \omega_\beta \mathcal{L}^0_{\alpha\beta\gamma\delta} \, \Delta v_\gamma = \eta^2 \Delta \ddot{v}_\alpha \,, \tag{2.17}$$

$$-\omega_\delta \omega_\beta \mathcal{L}^0_{\alpha\beta\gamma\delta} \, \Delta u_\gamma = \eta^2 \Delta \dot{v}_\alpha \,. \tag{2.18}$$

Substituting the $\Delta\mathbf{u}$ terms in (2.17) from (2.18), one obtains an equation expressed only in terms of $\Delta\mathbf{v}$

$$\eta^2 \frac{\partial \mathcal{L}_{\alpha\beta\epsilon\zeta}}{\partial F_{\gamma\delta}}\bigg|_0 \dot{F}^0_{\epsilon\zeta} \, \omega_\delta \omega_\beta \left[ \mathcal{L}^0_{\gamma\eta\xi\theta} \, \omega_\eta \omega_\theta \right]^{-1} \Delta \dot{v}_\xi - \omega_\beta \omega_\delta \mathcal{L}^0_{\alpha\beta\gamma\delta} \, \Delta v_\gamma = \eta^2 \Delta \ddot{v}_\alpha \,. \tag{2.19}$$

Denoting the magnitude of the Fourier transform variable $\boldsymbol{\omega}$ by $\omega \equiv \sqrt{\omega_1^2 + \omega_2^2}$ and its orientation by $\mathbf{n}$ ($n_1 = \cos\phi$, $n_2 = \sin\phi$), allows us to rewrite (2.19) as

$$-M_{\alpha\gamma}(\phi) \, \Delta \dot{v}_\gamma + (\omega/\eta)^2 A_{\alpha\gamma}(\phi) \Delta v_\gamma + \Delta \ddot{v}_\alpha = 0 \,, \tag{2.20}$$

with the $\phi$-dependent acoustic tensor $\mathbf{A}(\phi)$ defined in (2.7) and the damping tensor $\mathbf{M}(\phi)$ defined by

$$M_{\alpha\xi}(\phi) \equiv \frac{\partial \mathcal{L}_{\alpha\beta\epsilon\zeta}}{\partial F_{\gamma\delta}}\bigg|_0 \dot{F}^0_{\epsilon\zeta} \, n_\beta n_\delta \, A^{-1}_{\gamma\xi}(\phi) \,. \tag{2.21}$$

For a hyperelastic solid,[10] we can express $\mathbf{M}(\phi)$ in terms of $\mathbf{A}(\phi)$. In this special case, the plane-stress incremental moduli tensor is derived from the energy density $W$ by (2.6), and thus one has from (2.21)

$$M_{\alpha\xi} = \frac{\partial^3 W}{\partial F_{\alpha\beta}\partial F_{\epsilon\zeta}\partial F_{\gamma\delta}}\bigg|_0 \dot{F}^0_{\epsilon\zeta}\, n_\beta n_\delta\, A^{-1}_{\gamma\xi} = \frac{d}{d\tau}\Big(\mathcal{L}_{\alpha\beta\gamma\delta}\, n_\beta n_\delta\Big) A^{-1}_{\gamma\xi} = \dot{A}_{\alpha\gamma}\, A^{-1}_{\gamma\xi}\,. \tag{2.22}$$

Next we "*freeze*" the coefficients to their values at $\tau_0$ and introduce $\delta\mathbf{y} \equiv (\delta\mathbf{v}, \delta\dot{\mathbf{v}})$ to rewrite the system in (2.20) (using also (2.22)) as a first order constant coefficient system

$$\mathbf{C}\,\delta\mathbf{y} = \delta\dot{\mathbf{y}}\,; \quad \mathbf{C} \equiv \begin{bmatrix} \mathbf{0} & \mathbf{I} \\ -(\omega/\eta)^2\mathbf{A} & \dot{\mathbf{A}}\mathbf{A}^{-1} \end{bmatrix}, \quad \delta\mathbf{y} \equiv \begin{bmatrix} \delta\mathbf{v} \\ \delta\dot{\mathbf{v}} \end{bmatrix}$$
$$\Longrightarrow \quad \delta\mathbf{y}(\tau) = \exp[\mathbf{C}(\tau - \tau_0)]\delta\mathbf{y}(\tau_0)\,. \tag{2.23}$$

Sufficient conditions for the stability of the linearized perturbation problem in Fourier space $\boldsymbol{\omega}$ in (2.23) at the neighborhood of $\tau_0$ are met when all eigenvalues $s_I$ of the matrix $\mathbf{C}$ have negative real parts,[11] i.e., $\Re[s_I] < 0$. It will be shown that this requirement also results in sufficient stability conditions in the original $\boldsymbol{\chi}$ space.

The system (2.23) has a solution of the form

$$\Delta\mathbf{v}(\boldsymbol{\omega}, \tau) = \sum_{I=1}^{4} \xi_I(\boldsymbol{\omega}) \exp\left[s_I(\boldsymbol{\omega})(\tau - \tau_0)\right] \mathbf{V}^I(\boldsymbol{\omega})\,, \tag{2.24}$$

where $s_I$ are the four eigenvalues of $\boldsymbol{C}$ and $\mathbf{V}^I$ the corresponding eigenvectors satisfying

$$\mathrm{Det}\left[-s_I\dot{\mathbf{A}}\mathbf{A}^{-1} + (\omega/\eta)^2\mathbf{A} + s_I^2\mathbf{I}\right] = 0\,, \quad \left[-s_I\dot{\mathbf{A}}\mathbf{A}^{-1} + (\omega/\eta)^2\mathbf{A} + s_I^2\mathbf{I}\right]\mathbf{V}^I = \mathbf{0}\,. \tag{2.25}$$

The amplitudes $\xi_I(\boldsymbol{\omega})$ appearing in (2.24) are computed with the help of initial conditions

$$\Delta\mathbf{v}(\boldsymbol{\omega}, \tau_0) = \sum_{I=1}^{4} \xi_I(\boldsymbol{\omega})\mathbf{V}^I(\boldsymbol{\omega})\,, \quad \Delta\dot{\mathbf{v}}(\boldsymbol{\omega}, \tau_0) = \sum_{I=1}^{4} \xi_I(\boldsymbol{\omega}) s_I(\boldsymbol{\omega})\mathbf{V}^I(\boldsymbol{\omega})\,, \tag{2.26}$$

where $\Delta\dot{\mathbf{v}}(\boldsymbol{\omega}, \tau_0)$ is given in terms of $\Delta\mathbf{u}(\boldsymbol{\omega}, \tau_0)$ from (2.18).

The sought solution of the perturbed plate in the original $\boldsymbol{\chi}$ space is obtained by Fourier inversion of (2.24)

$$\delta\mathbf{v}(\boldsymbol{\chi}, \tau) = \frac{1}{2\pi}\int_{\mathbb{R}^2} \sum_{I=1}^{4} \left\{\xi_I(\boldsymbol{\omega}) \exp\left[s_I(\boldsymbol{\omega})(\tau - \tau_0) - i\boldsymbol{\omega}\cdot\boldsymbol{\chi}\right]\mathbf{V}^I(\boldsymbol{\omega})\right\} d\boldsymbol{\omega}\,. \tag{2.27}$$

The stability of the system (2.23) follows from (2.27) when $\Re[s_I] < 0$.

A sufficient condition for the matrix $-\dot{\mathbf{A}}\mathbf{A}^{-1} + (\omega/\eta)^2\mathbf{A}$ to be positive definite for $\tau < \tau_m$ and for all $(\omega/\eta)$, is when $-\dot{\mathbf{A}}$ is positive definite, since by construction $\mathbf{A}(\tau, \phi)$ is positive definite for $0 \le \tau < \tau_m$. Since from (2.10) as the dimensionless time $\tau$ increases $\mathbf{A}(\tau, \phi)$

[10] Linearized stability is studied here only for a hyperelastic material; for the other constitutive laws only numerical calculations are available, which nevertheless confirm our findings for the hyperelastic case.

[11] The matrix $\mathbf{C}$ has all eigenvalues with negative real part iff $(\omega/\eta)^2\mathbf{A} - \dot{\mathbf{A}}\mathbf{A}^{-1}$ is positive definite (e.g., see [2]).

loses its positive definiteness at $\tau_e(\phi)$ for each direction $\phi$, for the constitutive laws adopted in this work $-\dot{\mathbf{A}}(\tau, \phi)$ is positive definite for $0 \leq \tau < \tau_L$ where $\tau_L \leq \tau_m$ [12] is the dimensionless "*stability limit*" time.

Recall that linearized stability analysis predicts that – in the absence of loading rate or viscoplastic effects – all perturbations at $\tau_0 < \tau_m$ are stable, regardless of wavelength (e.g., [29]). Our result establishes that localized perturbations are linearly stable as long as $0 \leq \tau_0 < \tau_L$, where the stability limit time $\tau_L$ can be lower than the critical time $\tau_m$. Notice that if we do not require linearized stability for all $(\omega/\eta)$, the stability limit time $\tau_L$ can get closer to the critical time $\tau_m$.

### 2.3 Initial Stability (Transient Growth)

The linearized stability investigated in the previous section pertains to the evolution (assuming constant coefficients) of perturbations for large times after their onset, i.e., for $\tau \gg \tau_0$. More relevant to the physical system is the initial response of the plate to perturbations, i.e., the initial growth rate at $\tau = \tau_0$. This is the concept of "*transient growth*" used frequently in fluid mechanics, e.g., see [25], where a Lyapunov stable flow can exhibit a significant initial amplification of the perturbation.

It is possible for the case of a Lyapunov stable matrix $\mathbf{C}$, certain values of an initial perturbation $\delta\mathbf{y}(\tau_0)$ will encounter a significant initial amplification of the $\|\delta\mathbf{y}(\tau)\|$ before its eventual decay. Unfortunately there is no formula for the maximum of $\|\delta\mathbf{y}(\tau)\|$ but it is possible to calculate the very short time behavior of the linearized system in (2.23).

The maximum possible growth rate at short times is given by the initial derivative of the norm $\|\exp[\mathbf{C}(\tau - \tau_0)]\|$. Using the definition of the norm of a matrix and the approximation near $\tau_0$ of $\exp[\mathbf{C}(\tau - \tau_0)] \approx \mathbf{I} + \mathbf{C}(\tau - \tau_0) + O(\tau - \tau_0)^2$

$$\|\exp[\mathbf{C}(\tau - \tau_0)]\|^2 \equiv \max_{\|\mathbf{x}\|=1} \frac{\|\exp[\mathbf{C}(\tau - \tau_0)]\mathbf{x}\|^2}{\|\mathbf{x}\|^2} \approx 1 + \max_{\|\mathbf{x}\|=1} \frac{\mathbf{x}^T(\mathbf{C}^T + \mathbf{C})\mathbf{x}}{\mathbf{x}^T\mathbf{x}}(\tau - \tau_0) \implies$$
$$\implies \left.\frac{d\|\exp[\mathbf{C}(\tau - \tau_0)]\|^2}{d\tau}\right|_{\tau_0} = \left[\max_{\|\mathbf{x}\|=1} \frac{\mathbf{x}^T[(\mathbf{C}^T + \mathbf{C})]\mathbf{x}}{\mathbf{x}^T\mathbf{x}}\right] = \text{max eigenvalue of } (\mathbf{C}^T + \mathbf{C})\,. \tag{2.28}$$

The maximum possible growth rate at short times, is thus given by $\mu$, the largest (real) eigenvalue of the symmetric matrix $(\mathbf{C} + \mathbf{C}^T)$. From the definition for $\mathbf{C}$ in (2.23) one has the following characteristic equation for $\mu$

$$\det[-\mu(\dot{\mathbf{A}}\mathbf{A}^{-1} + \mathbf{A}^{-T}\dot{\mathbf{A}}^T) - [(\mathbf{I} - (\omega/\eta)^2\mathbf{A})]^2 + \mu^2\mathbf{I}] = 0$$
$$\implies \quad c_4\mu^4 + c_3\mu^3 + c_2\mu^2 + c_1\mu + c_0 = 0\,. \tag{2.29}$$

A perturbation is termed "*initially stable*" if $\mu < 0$. According to the Routh-Hurwitz theorem a necessary condition for $\mu < 0$ is that the fourth order polynomial (2.29) has all positive coefficients $c_i$. However, unlike the roots $s_I$ of $(2.25)_1$ it can be shown for the current problem that the coefficient $c_1 < 0$. Thus we conclude that the plate is initial unstable for at least some initial perturbations at any time $\tau$. For a more reliable picture on the dynamic stability of the plate one has to perform numerical calculations for the fully nonlinear problem.

[12] This inequality is verified by the numerical calculations in Appendix C.

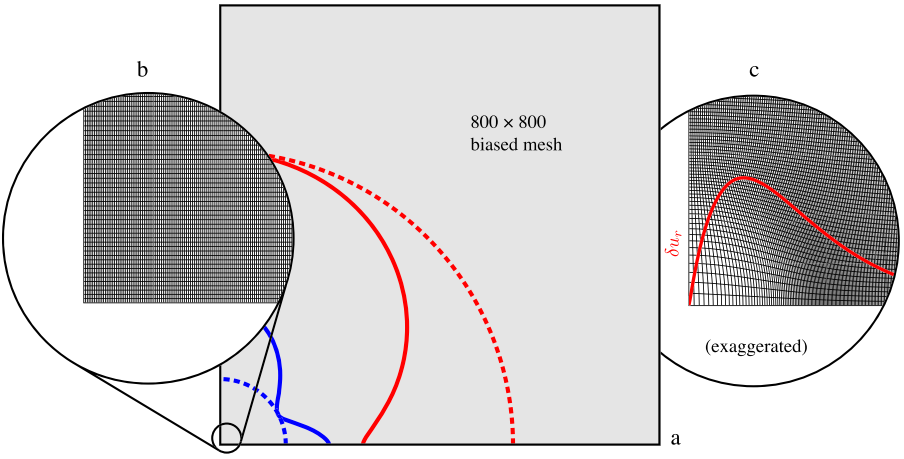


**Fig. 3** In **a**) is depicted the domain $\mathcal{D}$ (reference configuration) used for the FEM calculations of the evolution of a spatially localized perturbation at $\boldsymbol{\chi} = \mathbf{0}$, introduced at different dimensionless times $\tau$. From symmetry, only the quadrant $\chi_1 > 0$, $\chi_2 > 0$ is used. The mesh consists of rectangular quads with aspect ratio $\tan(\phi_m)$. Also plotted are the influence zones (in solid blue line for the slower $v_-$ and in solid red line for the faster $v_+$ wave speeds) at time $\tau_m$, corresponding to the first loss of ellipticity, as well as the corresponding $\delta_-$ (in dashed blue line) and $\delta_+$ (in dashed red line) influence discs at $\tau_m$. The domain of calculation is considerably larger than the influence disc $\delta_+$, thus ensuring no influence of boundary conditions for times exceeding $1.5\tau_m$ even for perturbations introduced at $\tau = 0$. The insert **b**) shows the undistorted mesh near the origin used for a velocity perturbation while the insert **c**) shows the corresponding (exaggerated) locally distorted mesh at the onset of a displacement perturbation

## 2.4 Nonlinear Stability

Having established the linearized stability analysis of the frozen-coefficient problem, the next step is to investigate the nonlinear stability of a single spatially localized perturbation at $\boldsymbol{\chi} = \mathbf{0}$ – in either displacement or velocity – triggered at different times $\tau$. The analysis is done using the simplest constitutive law, namely the hyperelastic, finite (logarithmic) strain model with a uniaxial power law, given in Appendix A. The use of this model for elastoplastic materials is justified by the initially small deviations from proportional loading and the absence of unloading in these calculations which, as it will be subsequently verified, occurs well after the onset of loss of ellipticity at $\tau_m$. Since no analytical solution is possible, a numerical FEM-based algorithm is used, described in [29].

From symmetry considerations only the positive quadrant $\chi_1 > 0$, $\chi_2 > 0$ of the domain $\mathcal{D}$ is used in the calculations for a spatially localized perturbation or imperfection, while the entire domain $\mathcal{D}$ is used for calculating the interaction of imperfections. The spatial discretization of the plate employs standard two-dimensional isoparametric quadrilateral elements with aspect ratio $\tan(\phi_m)$. The boundary conditions imposed at any time are the displacements and velocities of the principal (perfect) solution given in (2.1) at the sides $\chi_1 > 0$, $\chi_2 > 0$ and the zero normal displacements and velocities at the sides $\chi_1 = 0$, $\chi_2 = 0$ or the displacements and velocities of the principal (perfect) solution at all sides, for calculating the interaction of imperfections. The rectangular, reference configuration domain used in the calculations largely exceeds a disc of radius $\delta_+$, as seen in Fig. 3, thus ensuring that no perturbation wave ever reaches any boundary for times exceeding $1.5\tau_m$. The mesh used consists of $800 \times 800$ elements. The initial conditions are the displacements and velocities of the principal solution (2.1).

For the case of a single, spatially localized displacement (or velocity) perturbation with an amplitude parameter $\xi$, we use the following expression in polar coordinates

$$\delta u_r = \xi r \exp(-r/R)\ ,\ \delta u_\theta = 0\,; \quad (\,\delta v_r = \xi r \exp(-r/R)\ ,\ \delta v_\theta = 0\,)\,. \tag{2.30}$$

An (exaggerated) depiction of the perturbed mesh near the origin, for both velocity and displacement cases, is shown in Fig. 3. At onset time $\tau_0$, the radial component of the perturbation is maximized at $r = R$ and decays exponentially for $r > R$. We can thus refer to $R$ as the "*size*" of the spatially localized perturbation, which is the same in all the following calculations and has a value: $R = 10^{-2}$. To avoid mesh inversion one must ensure that $d(r + u_r^0 + \delta u_r)/dr > 0$, which implies from (2.30) that $\xi < (1 + \tau_0)\mathrm{e}^2)$.

Details of the perturbations used and the special element – incorporating the constitutive law and time solution algorithm – introduced in the commercial FEM code (ABAQUS) to calculate the results are given in [29].

## 3 Results

This section starts by presenting the nonlinear stability analysis of the plate through the time evolution of a spatially localized perturbation of various amplitudes introduced at different times $\tau_0$. The investigation of a spatially localized imperfection, introduced at the onset of loading (i.e., at $\tau_0 = 0$) is presented next, showing the dynamic delay of localization (deformation patterns for times $\tau > \tau_m$), followed by the influence of unloading and ending with the study of interaction of several such imperfections of random location and strength. All calculations are performed for a loading rate parameter $\eta = 1$ – defined in (2.9) – corresponding to a mechanical (transverse) loading rate equal to the (axial) wave propagation speed.

### 3.1 Time Evolution of Spatially Localized Perturbations

Following the linearized stability analysis for a perturbation in Sect. 2.2, we present next in Fig. 4 to Fig. 6 the numerical results for the nonlinear stability problem by following the evolution of a single, spatially localized perturbation – in velocity or displacement – triggered at different times $\tau_0$.

Starting in Fig. 4, we show the amplitude evolution of a spatially localized (about $\boldsymbol{\chi} = \mathbf{0}$) velocity perturbation introduced at different (dimensionless) times $\tau_0$, before or after $\tau_m$ (indicated by a dotted vertical line). The measure of the perturbation amplitude $\|\delta\mathbf{v}\|$ is the $L_2$ norm (squared) of the difference in velocities, between the perturbed and unperturbed (spatially uniform) solutions, defined in (2.14)

$$\|\delta\mathbf{v}\| \equiv \int_{\mathcal{D}} \{[v_1(\boldsymbol{\chi},\tau) - v_1^0(\boldsymbol{\chi})]^2 + [v_2(\boldsymbol{\chi},\tau) - v_2^0(\boldsymbol{\chi})]^2\} dA\,. \tag{3.1}$$

The perturbation amplitude is calculated numerically, over the entire domain $\mathcal{D}$, using one Gauss point per element. Calculations are presented for a hyperelastic material with a power-law uniaxial response ($n = 0.22$ and $\epsilon_y = 0.002$) for three different loading angles: $\psi = -\pi/12$,[13] (left column), $\psi = 0$, (central column) and $\psi = \pi/4$, (right column) and for

[13] Best approximation of uniaxial stress under strain control, corresponding to an initial uniaxial stress $\sigma_1 \neq 0$, $\sigma_2 = 0$. From (A.16) one has $\epsilon_2 = -\epsilon_1/2$; for small strain $\epsilon_i \approx \lambda_i - 1$, resulting in $\psi = -\pi/12$ according to (2.1).

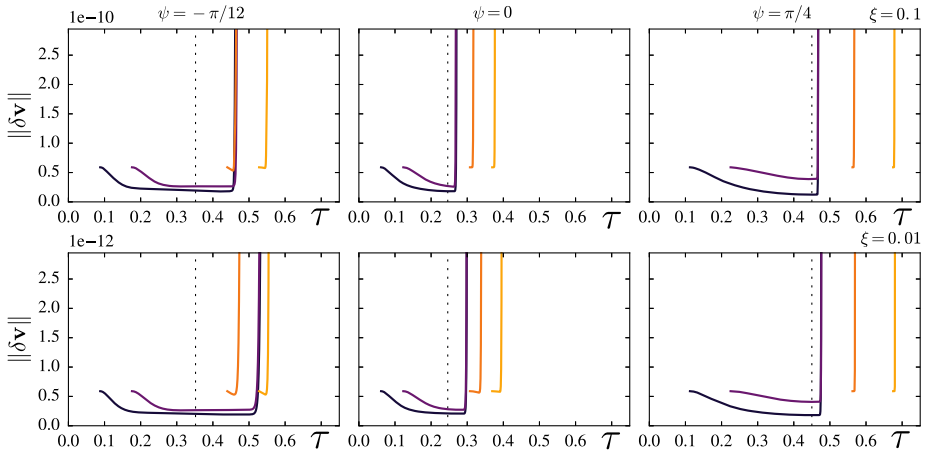


**Fig. 4** Amplitude evolution of a spatially localized (about $\boldsymbol{\chi} = \mathbf{0}$) velocity perturbation for a mechanical loading rate commensurate with the wave propagation speed ($\eta = 1$), introduced at different (dimensionless) times $\tau_0$. Calculations are presented for a hyperelastic material with a power-law uniaxial response ($n = 0.22$) for three different loading angles and for two different perturbation amplitude parameters, as indicated. The dotted vertical line marks the critical and stability limit times ($\tau_m = \tau_L$)

two different perturbation amplitude parameters, defined in (2.30): $\xi = 0.1$ (top row) and $\xi = 0.01$ (bottom row). From the calculations in Appendix C, and according to (C.5) for the hyperelastic material with a hardening exponent $n = 0.22$, the stability limit time coincides with the critical time, i.e., $\tau_L = \tau_m$ for all the loading angles considered in Fig. 4.

As expected from the linearized analysis in Sect. 2.2, the amplitude of a perturbation introduced at $\tau_0 < \tau_m$ starts by decreasing monotonically. As time progresses, it reaches a plateau and does not increase again until after some time $\tau > \tau_m$, depending on load orientation $\psi$ and amplitude parameter $\xi$. This is somewhat analogous to the delay in necking strain observed in modal analyses (e.g., [8, 10, 22]), where the delay in the onset of a rapid growth of the perturbation decreases with increasing perturbation amplitude, as seen here in Fig. 5. Unfortunately a direct comparison with our results is not possible, since their work – unlike ours – is based on rate-dependent constitutive laws.

Perturbations introduced at times $\tau_0 > \tau_m$ show a very steep growth with an almost vertical take-off. For the smaller perturbation amplitude parameter $\xi = 0.01$, the very small initial decay before the explosive growth of perturbations initiated at $\tau_0 > \tau_m$ is due to the norm choice adopted[14] and essentially disappears for $\xi = 0.1$. A perturbation introduced at $\tau_0 < \tau_m$ remains "*dormant*" under dynamic straining until the macroscopic strains of the plate exceed those corresponding to the onset of the first loss of ellipticity under static loading conditions. Notice that for a load orientation $\psi = -\pi/12$ and the smaller initial perturbation amplitude parameter $\xi = 0.01$, this delay can be quite remarkable. Another interesting feature of the nonlinear perturbation analysis is that the retarded (occurring for $\tau > \tau_m$) explosive growth of a perturbation initiated at $\tau_0 < \tau_m$, is independent of the time of its initiation, but starts closer to $\tau_m$ as the perturbation amplitude parameter increases.

The amplitude evolution of a spatially localized (about $\boldsymbol{\chi} = \mathbf{0}$) displacement perturbation introduced at different (dimensionless) times $\tau_0$, before or after $\tau_m$ (indicated by a dotted

[14] A norm choice involving both displacements and velocities could be used but the choice made here is judged more physically appropriate.

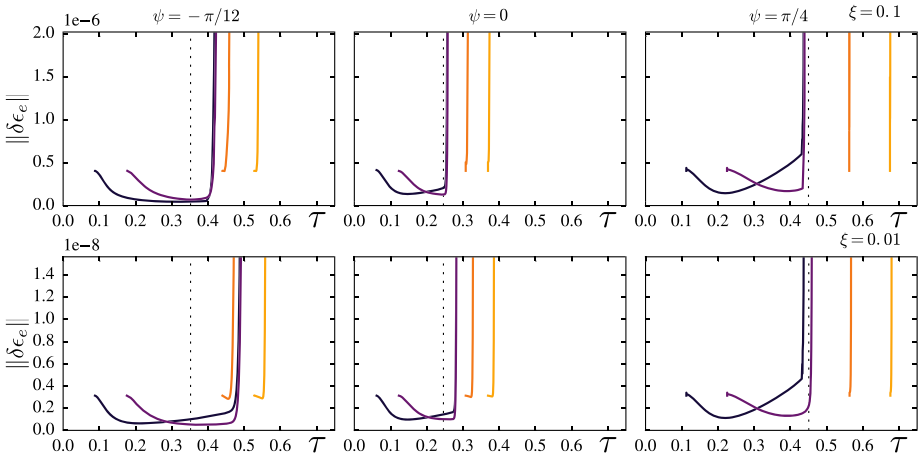


**Fig. 5** Amplitude evolution of a spatially localized (about $\boldsymbol{\chi} = \mathbf{0}$) displacement perturbation for a mechanical loading rate commensurate with the wave propagation speed ($\eta = 1$), introduced at different (dimensionless) times $\tau_0$. Calculations are presented for a hyperelastic material with a power-law uniaxial response for three different loading angles and for two different perturbation amplitude parameters, as indicated. The dotted vertical line marks the critical and stability limit times ($\tau_m = \tau_L$)

vertical line) is depicted in Fig. 5. In this case, the measure of the perturbation amplitude $\|\delta\epsilon_e\|$ is the $L_2$ norm (squared) of the difference in the equivalent logarithmic strain $\epsilon_e$, given in (A.14)$_3$, between the perturbed and unperturbed (spatially uniform) solutions:

$$\|\delta\epsilon_e\| \equiv \int_{\mathcal{D}} [\epsilon_e(\boldsymbol{\chi}, \tau) - \epsilon_e^0(\tau)]^2 dA \,. \tag{3.2}$$

The perturbation amplitude is again calculated numerically as discussed for (3.1). Calculations are presented for a hyperelastic material with the same power-law uniaxial response, loading angles and initial perturbation amplitude parameters as in Fig. 5, giving similar results: perturbations initiated at $\tau_0 < \tau_m$ exhibit an initial decay in amplitude, while perturbations initiated at $\tau_0 > \tau_m$ show a steep growth in amplitude with an almost vertical take-off.

Some differences are also observed. For $\tau_0 < \tau_m$, the initial decay of the perturbation's amplitude eventually terminates and is followed by a slow growth (no plateau found as in Fig. 4) until the macroscopic strains of the plate exceed those corresponding to the onset of the first loss of ellipticity; an unbounded growth of the perturbation amplitude follows, either near $\tau_m$ or well past it, as seen in Fig. 5 for the case of a loading angle $\psi = -\pi/12$ and in particular for the smaller perturbation amplitude parameter $\xi = 0.01$. The same remark as before can also be made for the displacement perturbation: a small perturbation remains inconsequential in a dynamic loading until the macroscopic strains of the plate are well past those corresponding to the loss of ellipticity under static loading conditions.

Having investigated the influence of load orientation $\psi$ and amplitude parameter $\xi$ on the nonlinear stability of a spatially localized perturbation, of interest is next the influence of the (hyperelastic) constitutive law, as measured by the equivalent uniaxial response's power law exponent $n$ defined in (A.13). We show in Fig. 6 the time evolution of amplitude $\|\delta\epsilon_e\|$ of a spatially localized (about $\boldsymbol{\chi} = \mathbf{0}$) displacement perturbation introduced at different (dimensionless) times $\tau_0$, before or after $\tau_L$. Calculations are presented for two different exponents of the power law uniaxial response, ($n = 0.22$ left and $n = 0.40$ right), a loading angle $\psi = -\pi/12$ and initial perturbation amplitude parameter $\xi = 0.01$.

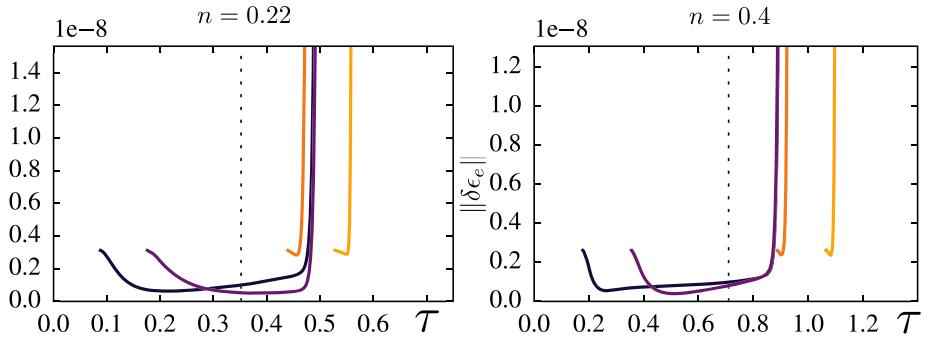


**Fig. 6** Influence of constitutive law (hyperelastic), as measured by the hardening exponent $n$ of the power-law uniaxial response, on the amplitude evolution of a spatially localized (about $\boldsymbol{\chi} = \mathbf{0}$) displacement perturbation for a mechanical loading rate commensurate with the wave propagation speed ($\eta = 1$), introduced at different (dimensionless) times $\tau_0$ for a loading angle $\psi = -\pi/12$. The dotted vertical line marks the corresponding critical time $\tau_m$. For $n = 0.22$, $\tau_m = \tau_L = 0.352$ while for $n = 0.4$, $\tau_m = 0.715 > \tau_L = 0.475$

Apart from the fact that the stiffer plate ($n = 0.40$) has a larger stability limit time $\tau_L$ than its softer counterpart ($n = 0.22$), the stability results are conforming to the expectations from the linearized analysis: perturbations initiated at $\tau_0 < \tau_L$ exhibit an initial decay in amplitude, noticeably sharper for the stiffer plate ($n = 0.40$), while perturbations initiated at $\tau_0 > \tau_m$ show a steep growth in amplitude with an almost vertical take-off. Moreover, consistent with our previous findings in Fig. 4 and Fig. 5, we note that a perturbation introduced at $\tau_0 < \tau_L$ remains "*dormant*" under dynamic straining until the macroscopic strains of the plate are well past those corresponding to the onset of the first loss of ellipticity under static loading conditions at $\tau_m$; the time at which the explosive growth occurs is independent of the time at which these perturbations were introduced.

The numerical calculations for the nonlinear stability problem confirm the prediction of the linearized analysis, i.e., that perturbations initiated at $\tau_0 < \tau_L$ show an initial decay and are thus stable near the time of perturbation onset. An even more interesting trend is found: a small perturbation remains inconsequential under dynamic loading conditions until the macroscopic strains of the plate well exceed those corresponding to the onset of the first loss of ellipticity under static loading conditions at $\tau_m$; the smaller the initial perturbation or the closer the load orientation is to uniaxial tension, the larger is this delay.

### 3.2 Dynamic Delay in the Evolution of Spatially Localized Imperfections

Following the study of spatially localized perturbations introduced at different times $\tau_0$, attention is turned next to the evolution of spatially localized "*imperfections*", i.e., defects in the material properties of the plate introduced at $\tau_0 = 0$. The information provided in Fig. 7 to Fig. 12 shows the propagation of the localized deformation "*tongues*" at different dimensionless times. This is an alternative way to visualize the delay between static localization, where the statically loaded uniformly strained perfect plate will show the development of a strongly localized necking pattern as $\tau_m$ is approached (see [1]), while its dynamically loaded counterpart continues to deform uniformly for $\tau > \tau_m$, i.e., for strains above those corresponding to the loss of ellipticity, outside the region of localized deformation.

To simulate an imperfection, we use an element (the one containing the origin) with a slightly different shear modulus, i.e., $G(1 + \zeta)$, where $\zeta$ is the imperfection amplitude parameter. The influence of what is essentially a point defect at the origin, will be studied

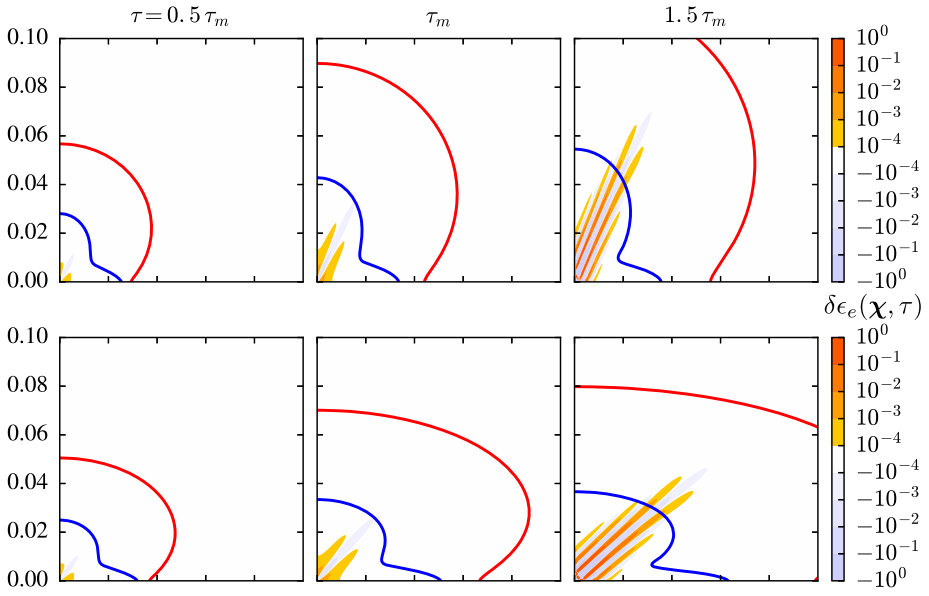


**Fig. 7** Equivalent strain change contours $\delta\epsilon_e(\boldsymbol{\chi}, \tau)$ due to a spatially localized (about $\boldsymbol{\chi} = \mathbf{0}$) imperfection with an amplitude parameter $\zeta = 0.01$ introduced at $\tau = 0$ are plotted in the reference configuration (top row) and in the current configuration (bottom row) at three dimensionless times, calculated for a mechanical loading rate commensurate with the wave propagation speed ($\eta = 1$). The graphs at $\tau = 1.5\tau_m$ clearly indicate the dynamic delay in the localized deformation pattern. The extent of the influence zones corresponding to the slower $v_-$ and faster $v_+$ wave speeds at these three times are also recorded. Results calculated for a hyperelastic material with a piecewise power law, a uniaxial curve hardening exponent $n = 0.22$ and a loading angle $\psi = -\pi/12$. The same scale is used in both directions in each plot

by following the evolution with respect to time of the spatial change of the difference in equivalent strain between the imperfect and perfect plates:

$$\delta\epsilon_e(\boldsymbol{\chi}, \tau) \equiv \epsilon_e(\boldsymbol{\chi}, \tau) - \epsilon_e^0(\tau)\,, \tag{3.3}$$

where the equivalent logarithmic strain $\epsilon_e$ is defined in $(A.14)_3$. The results are presented in Fig. 7 to Fig. 12, where the same scale is used in both spatial directions of each plot.

The influence of spatially localized (about $\boldsymbol{\chi} = \mathbf{0}$) imperfection on the development of a localized deformation zone in a rapidly strained plate is presented in Fig. 7. The equivalent strain change contours $\delta\epsilon_e(\boldsymbol{\chi}, \tau)$ are plotted in the reference configuration (top row) and in the current configuration (bottom row) at three dimensionless times: $\tau = 0.5\tau_m$, left column, $\tau = \tau_m$, center column and $\tau = 1.5\tau_m$, right column, where only regions of $|\delta\epsilon_e| \geq 10^{-4}$ are shown in color. The extent of influence zones for the slower and faster wave speeds $v_-$ and $v_+$ respectively, are also shown. Results are calculated for an imperfection amplitude parameter $\zeta = 0.01$ and correspond to a hyperelastic constitutive law with a piecewise power law uniaxial curve ($n = 0.22$, $\epsilon_y = 0.002$) and a loading angle $\psi = -\pi/12$.

For the lowest dimensionless time $\tau = 0.5\tau_m$, only a small region near the origin is affected, while at the time of onset of loss of ellipticity $\tau = \tau_m$, the localized deformation band is clearly visible at an angle $\pi/2 - \phi_m$ with respect to the $\chi_1$-direction, since the normal to the band forms an angle $\phi_m$ with respect to the $\chi_1$-direction, as defined in (2.11).

Notice that the localized deformation appears to propagate in three "*tongues*", as seen in the middle graphs of Fig. 7. This phenomenon can be explained by the rectangular shape of the initial imperfection domain, where each corner acts as a source of perturbation signals. A static analogue of this phenomenon has been found in [1]. Moreover due to wave propagation, the width of the localized deformation zone, obtained from fully nonlinear calculations, is considerably larger than the width of the initial imperfection, but also a fraction of the linearized estimate $\delta_-$ (influence disc for the slower wave) for the same time, a phenomenon also observed in the growth of a localized imperfection in the nonlinear bar model of [20].

At time $\tau = 1.5\tau_m$ the number of localized deformation "*tongues*" increases as does the corresponding maximum strain, which now reaches $|\delta\epsilon_e| \approx 1$. It is worth noting that the width of these localized deformation "*tongues*" remains unchanged; the localized deformation zone remains well within the influence zone corresponding to the fastest wave speed $v_+$; recall that the domain used for the numerical calculations is large enough as to preclude any signal reaching its boundary up to the maximum time considered.

The evolution of the imperfection's localized deformation zones in the current configuration is presented in the bottom row of Fig. 7. Due to the applied macroscopic loading (see (2.1)), the load orientation angle of $\psi = -\pi/12$ corresponds to a straining of the plate in the $\chi_1$-direction and a shortening along the $\chi_2$-direction, thus explaining the tilting of the plate's localized deformation "*tongues*" in clockwise direction. It should also be mentioned here that the entire specimen is not shown for the plots in the current configuration for better visual representation of the results.

The influence of the imperfection amplitude parameter $\zeta$ is examined next in Fig. 8, which shows the evolution of equivalent strain change contours $\delta\epsilon_e(\boldsymbol{\chi}, \tau)$ in a rapidly strained plate due to a spatially localized (about $\boldsymbol{\chi} = \mathbf{0}$) imperfection. The equivalent strain change contours $\delta\epsilon_e(\boldsymbol{\chi}, \tau)$, resulting from the presence of what amounts to a point defect at the origin, are plotted in reference configuration for two different values of the imperfection amplitude parameter: $\zeta = 0.1$ (top row) and $\zeta = 0.01$ (bottom row) at three dimensionless times: $\tau = 0.5\tau_m$, left column, $\tau = \tau_m$, center column and $\tau = 1.5\tau_m$, right column, where only regions of $|\delta\epsilon_e| \geq 10^{-4}$ are shown in color. The extent of the influence zones for the slowest and fastest wave speeds $v_-$ and $v_+$ respectively, are also shown at these three different times. Results are calculated for a hyperelastic constitutive law with a piecewise power law uniaxial curve ($n = 0.22$, $\epsilon_y = 0.002$) and a loading angle $\psi = -\pi/12$.

In comparing top and bottom graphs in Fig. 8 at the same dimensionless time, we observe as expected that the larger imperfection amplitude parameter results in a larger region influenced by the imperfection (the lowest threshold of $|\delta\epsilon_e| \geq 10^{-4}$ used in recording the equivalent strain perturbations remains unchanged for the top and bottom row plots). The shape of the imperfection being the same between top and bottom row figures, the number of localized deformation "*tongues*" remains unchanged. Once again, the localized deformation zone for $\zeta = 0.1$ remains well within the influence zone corresponding to the fastest wave speed $v_+$.

### 3.3 The Influence of Unloading

Since in our calculations we use a deformation theory (hyperelastic) model, it is worth examining the relevance of this simplifying hypothesis for plasticity, by finding when unloading starts and checking that it does not occur too soon. As unloading criterion we use the sign of the rate of equivalent strain $\dot{\epsilon}_e$, calculated numerically by comparing the equivalent strain

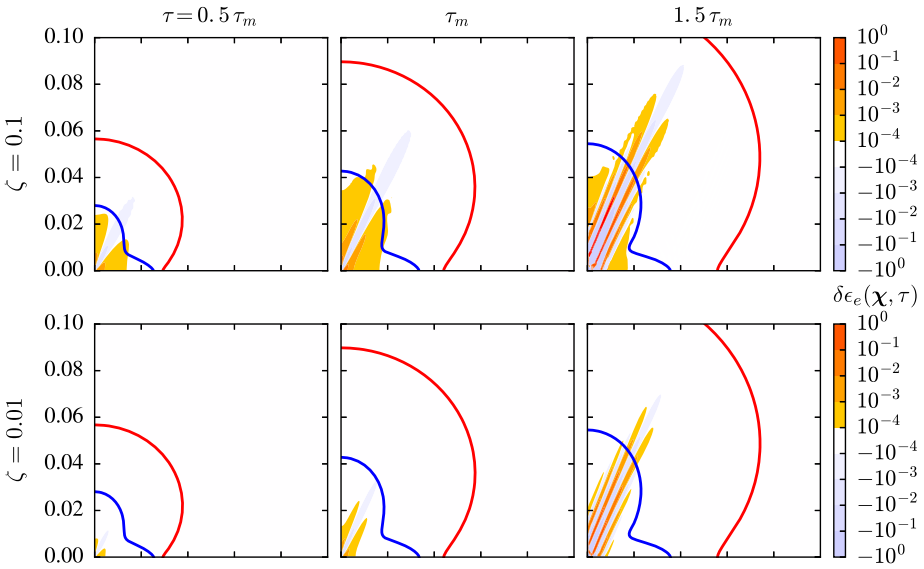


**Fig. 8** Equivalent strain change contours $\delta\epsilon_e(\boldsymbol{\chi}, \tau)$ due to a spatially localized (about $\boldsymbol{\chi} = \mathbf{0}$) imperfection introduced at $\tau = 0$ are plotted in the reference configuration for an imperfection amplitude parameter $\zeta = 0.1$ (top row) and an imperfection amplitude parameter $\zeta = 0.01$ (bottom row) at three dimensionless times, calculated for a mechanical loading rate commensurate with the wave propagation speed ($\eta = 1$). The graphs at $\tau = 1.5\tau_m$ clearly indicate the dynamic delay in the localized deformation pattern. The extent of the influence zones corresponding to the slower $v_-$ and faster $v_+$ wave speeds at these three times are also recorded. Results are calculated for a hyperelastic constitutive law with a piecewise power law uniaxial curve of hardening exponent $n = 0.22$ and a loading angle $\psi = -\pi/12$. The same scale is used in both directions in each plot

at the location in question between two subsequent time increments:

$$\dot{\epsilon}_e(\boldsymbol{\chi}, \tau) \approx [\epsilon_e(\boldsymbol{\chi}, \tau + \Delta\tau) - \epsilon_e(\boldsymbol{\chi}, \tau)]/\Delta\tau \tag{3.4}$$

The reference configuration unloading zone contours $\dot{\epsilon}_e < 0$ of a spatially localized (about $\boldsymbol{\chi} = \mathbf{0}$) imperfection are depicted in Fig. 9 at three dimensionless times past $\tau_m$: $\tau = 1.25\tau_m$, left column, $\tau = 1.5\tau_m$, middle column and $\tau = 1.75\tau_m$, right column, where only regions of $\dot{\epsilon}_e < 0$ are shown in color. The influence zones corresponding to the slower $v_-$ and faster $v_+$ wave speeds at these three times are also recorded. Results are calculated for an imperfection amplitude parameter $\zeta = 0.01$ and a hyperelastic constitutive law with a piecewise power law uniaxial curve with hardening exponent $n = 0.22$ (top row) and $n = 0.40$ (bottom row) for a loading angle $\psi = -\pi/12$.

Notice that no perceptible unloading appears in the imperfect plate at least up to $\tau = 1.25\tau_m$. For $\tau = 1.5\tau_m$ the unloading zones follow the localized deformation "*tongues*" shown in Fig. 7 and Fig. 8, while still remaining within the corresponding $v_-$ influence zone. The propagating *tongues* pattern breaks down at $\tau = 1.75\tau_m$ as a wide zone of the imperfect plate unloads. The results of these calculations show that at least up to $\tau = 1.25\tau_m$, the imperfect plate experiences no unloading and hence the equivalent strain change contours $\delta\epsilon_e(\boldsymbol{\chi}, \tau)$, resulting from the presence of what amounts to a point defect at the origin, are a reasonable approximation for an elastoplastic plate with the same uniaxial response, given the small deviations of the imperfect plate from proportional loading.

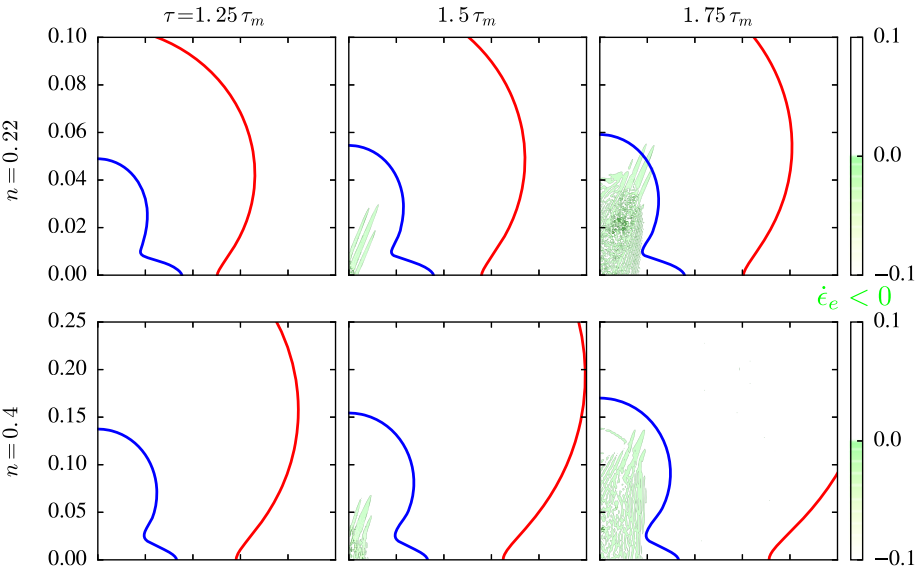


**Fig. 9** Reference configuration unloading zone contours $\dot{\epsilon}_e < 0$ of a spatially localized (about $\boldsymbol{\chi} = \mathbf{0}$) imperfection depicted at three dimensionless times past $\tau_m$, where only regions of $\dot{\epsilon}_e < 0$ are shown in color, calculated for a mechanical loading rate commensurate with the wave propagation speed ($\eta = 1$). The extent of the influence zones corresponding to the slower $v_-$ and faster $v_+$ wave speeds at these three times are also recorded. Results are calculated for a hyperelastic constitutive law with a piecewise power law uniaxial curve with hardening exponent $n = 0.22$ (top row) and $n = 0.40$ (bottom row) for a loading angle $\psi = -\pi/12$. The same scale is used in both directions in each plot

The question arising next is how the hyperelastic model results would compare with a more realistic plasticity model with the same uniaxial response. The calculations for this case are presented in Fig. 10, which shows the equivalent strain change contours $\delta\epsilon_e(\boldsymbol{\chi}, \tau)$, resulting from the presence of what amounts to a point defect at the origin, plotted in the reference configuration (top row) and the current configuration (bottom row) at three dimensionless times: $\tau = 0.25\tau_m$, left column, $\tau = \tau_m$, center column and $\tau = 1.75\tau_m$, right column, where only regions of $|\delta\epsilon_e| \geq 10^{-4}$ are shown in color. The extent of the influence zones for the slowest and fastest wave speeds $v_-$ and $v_+$ respectively, are also shown at different times in these figures. Results are calculated with an imperfection amplitude parameter $\zeta = 0.01$ for a $J_2$ flow theory elastoplastic constitutive law with a piecewise power law uniaxial curve ($n = 0.22$, $\epsilon_y = 0.002$) and a loading angle $\psi = -\pi/12$.

As expected from the much stiffer response of the $J_2$ flow theory (moduli given in (A.16) and (A.17)), the influence zones corresponding to $v_-$ and $v_+$ are considerably larger compared to their hyperelastic theory counterparts; notice that $v_+$ zone does not even appear in the graphs at $\tau_m$. The main difference between Fig. 7 and Fig. 10 is the consistency of the localized deformation "*tongues*" pattern that propagates along the characteristic direction but does not multiply the number of "*tongues*", thus producing a much narrower zone of localized deformation. Plasticity stabilizes the deformation pattern by concentrating deformation in a narrower zone (compared to its hyperelastic counterpart with the same uniaxial response) while relieving strains through unloading of the surrounding area.

The faster growth of the localized necking pattern in the hyperelastic material, compared to its elastoplastic counterpart with the same uniaxial response has also been observed in the work on ring fragmentation by [27]. The unloading feature of the elastoplastic model

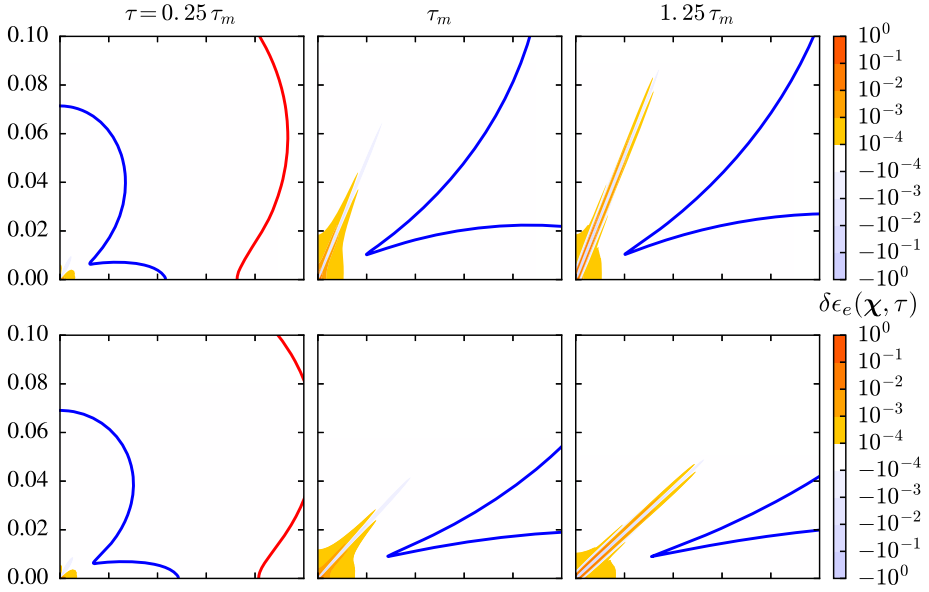


**Fig. 10** Equivalent strain change contours $\delta\epsilon_e(\boldsymbol{\chi}, \tau)$ due to a spatially localized (about $\boldsymbol{\chi} = \mathbf{0}$) imperfection are plotted in the reference configuration (top row) and in the current configuration (bottom row) at three dimensionless times, calculated for a mechanical loading rate commensurate with the wave propagation speed ($\eta = 1$). The influence zones corresponding to the slower $\nu_-$ and faster $\nu_+$ wave speeds are also shown in these figures. Results are calculated for an imperfection amplitude parameter $\zeta = 0.01$ and correspond to a $J_2$ flow theory elastoplastic constitutive law with a piecewise power law uniaxial curve ($n = 0.22$, $\epsilon_y = 0.002$) and a loading angle $\psi = -\pi/12$. The same scale is used in both directions in each plot

determines the later development of the localized pattern, as discussed in the following subsection.

### 3.4 Failure Pattern: Interaction of Imperfections

Since the ultimate failure pattern in rapidly strained solids depends on the interaction of (inevitable) defects, we calculate next the response of a plate under rapid biaxial straining with imperfections whose locations and strengths are distributed statistically; each imperfection consists of one element chosen randomly with an imperfection amplitude parameter $\zeta$ that varies with equal probability between 0% and 2%. Using the same imperfect plate, we present results for the hyperelastic model in Fig. 11 and for a $J_2$ flow theory elastoplastic model in Fig. 12, both sharing the same piecewise power law uniaxial curve ($n = 0.22$, $\epsilon_y = 0.002$). In each figure we plot, in the reference configuration, the equivalent strain change contours $\delta\epsilon_e(\boldsymbol{\chi}, \tau)$, resulting from the presence of the randomly distributed imperfections; only regions of $|\delta\epsilon_e| \geq 10^{-4}$ are shown in color.

Starting with the hyperelastic plate, observe that at $\tau = 0.5\tau_m$, prior to the onset of loss of ellipticity, there is no interaction between imperfections and only a small zone about them is influenced, as seen in the left graph of Fig. 11. At $\tau = \tau_m$ the deformation pattern shows a larger deviation from the perfect solution with neighboring imperfections linked by zones of localized deformation, but still no global localized deformation band appears. Only at $\tau = 1.5\tau_m$ a pattern of localized deformation bands appears that covers rather uniformly the entire domain.

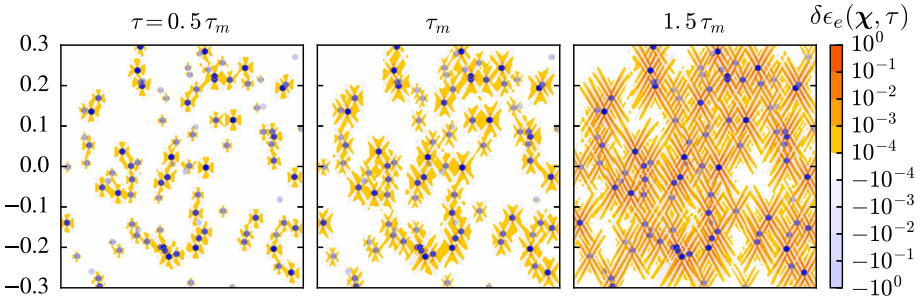


**Fig. 11** Reference configuration deformation pattern evolution in a biaxially strained hyperelastic plate with a random distribution of spatially localized imperfections shown at three times, calculated for a mechanical loading rate commensurate with the wave propagation speed ($\eta = 1$). Results correspond to piecewise power law uniaxial curve ($n = 0.22$, $\epsilon_y = 0.002$) and a loading angle $\tan\psi = -1/2$. The same scale is used in both directions in each plot

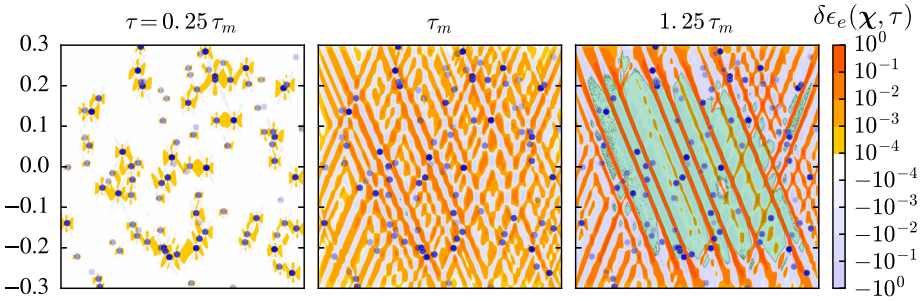


**Fig. 12** Reference configuration deformation pattern evolution in a biaxially strained $J_2$ flow theory elastoplastic plate with a random distribution of spatially localized imperfections shown at three times, calculated for a mechanical loading rate commensurate with the wave propagation speed ($\eta = 1$). Results correspond to piecewise power law uniaxial curve ($n = 0.22$, $\epsilon_y = 0.002$) and a loading angle $\tan\psi = -1/2$. Notice also the unloaded zones, depicted in green, that have appeared at time $\tau = 1.25\tau_m$. The same scale is used in both directions in each plot

Studying next the elastoplastic plate, we observe that at $\tau = 0.25\tau_m$, prior to the onset of loss of ellipticity, there is no interaction between imperfections and only a small zone about them is influenced as seen in the left graph of Fig. 12. At $\tau = \tau_m$ a deformation pattern appears with localized zones along the direction of loss of ellipticity that covers the entire plate. No unloading has yet appeared at this time. Finally at $\tau = 1.25\tau_m$ a smaller number of localized deformation bands with even higher strains appear that run across the entire plate and have $|\delta\epsilon_e| \approx 1$. Moreover a large part of the plate between these dominant bands experiences unloading conditions, thus explaining the strain concentration in a smaller number of such bands, compared to the case at $\tau = \tau_m$. We note that [34] performed a similar analysis on a quarter-symmetry elastoplastic tube model, with about 0.1% of randomly selected elements with a defect in the yield strength triggering localization.

By comparing the results in Fig. 11 and Fig. 12, one sees that although for some time prior to $\tau_m$, a deformation theory model is adequate to describe the initial evolution of randomly distributed defects, in order to understand the ultimate failure by localization it is important to use an elastoplastic constitutive law that properly accounts for elastic unloading. However, the deformation theory model shows clearly the delay in the development of

the localized deformation pattern for macroscopic strain states well past the dimensionless critical time $\tau_m$ corresponding to the onset of loss of ellipticity in the underlying constitutive model.

## 4 Conclusion

The issue of dynamic stability of structures and the associated failure patterns is an important engineering problem and as such has drawn considerable attention over the years. The commonly used approach to study localization phenomena (necking) in problems where inertia plays a dominant role, is the method of modal analysis which determines the structure's fastest growing eigenmode. This method, frequently combined with the assumption of a strain-rate-dependent material response, tacitly assumes that all points in the structure can be perturbed simultaneously, an assumption that is inappropriate for cases when the velocity of material points in the structure is comparable to the associated wave propagation speeds and leads to conclusions contradicted by experiments. In addition, the closely related problem of stability in dynamically loaded structures, i.e., the time evolution of perturbations introduced at different times during loading, does not seem to have attracted attention.

Motivated by the experimental studies of [32, 34] on the high strain-rate expansion of thin rings and tubes, that show no evidence of a dominant wavelength in their failure mode and no influence of strain-rate sensitivity on the necking strains, [20] addressed first the dynamic stability of an incompressible, nonlinearly elastic bar at different strain rates by following the evolution of spatially localized small perturbations introduced at different times. The same approach is adopted here for the dynamic stability of biaxially strained thin plates, following the work of [29], who defined the concept of influence discs and studied numerically the dynamic evolution of initial imperfections using rate-independent elasto-plastic constitutive laws. A dimensionless form of the governing equations is introduced together with the "*loading rate parameter*" $\eta$ that relates the transverse strain-rate to the axial wave propagation speed at zero strain.

An analytical method, based on linearization with frozen coefficients, is used to predict the initial stability of a *spatially localized imperfection*. We find that a perturbation is always stable if introduced at a time $\tau_0$ prior to the "*stability limit time*" $\tau_L$, the $\eta$-independent dimensionless time corresponding to the linear system's stability. This time is smaller than – or frequently coincides with – the "*critical time*" $\tau_m$, the also $\eta$-independent dimensionless time corresponding to the loss of ellipticity of the plate's constitutive law under static loading. It is worth noting that the concept of a stability limit time different than the critical time is novel and due to the two dimensionality of the plate problem, in contrast to the one dimensional bar problem studied in [20] when these two values coincide. Another interesting outcome of this investigation is that the plate is always *initially unstable* since an initial amplification of some perturbation is always possible.

Using a finite strain hyperelastic model,[15] we also calculate numerically – based on FEM and for mechanical loading rates commensurate to the wave propagation speed ($\eta = 1$) – the fully nonlinear time evolution problem of spatially localized perturbations, initiated at different times. The numerically obtained results are in agreement with the linearized analysis, which predicts that the plate is stable when perturbed at $0 < \tau_0 \leq \tau_L$. Moreover, we are able to calculate the dimensionless time delay, i.e., the dimensionless time $\tau > \tau_m$ required for

[15] A deformation theory type of plasticity based on logarithmic strain in the absence of unloading.

the unbounded growth of a spatially localized perturbation. It is found that this delay – important for the explanation of increased ductility in certain dynamically loaded structures, as in the case of electromagnetically expanded tubes in [34] – is almost insensitive to the time of introduction of the perturbation but very sensitive to its amplitude, the loading orientation and the constitutive law.

While the observed delay in the growth of the localized bands that might appear, at first sight, to be similar to the results in the literature based on modal analysis (e.g., see [8, 10]), the present work reveals that the delay occurs even when spatially localized perturbations are considered in the fully nonlinear problem with an evolving background state, and furthermore that inertia alone is sufficient to generate such delays in the growth of these localized perturbations.

The use of a finite strain hyperelastic theory of plasticity model to study the evolution of spatially localized perturbations and imperfections is found to be appropriate, since unloading is detected only well past the time corresponding to the loss of ellipticity in the perfect plate. Since the ultimate failure pattern depends on the interaction of statistically distributed defects, as argued in [34], cases of plates with statistically distributed initial imperfections are also presented. These calculations use a hyperelastic as well as an elastoplastic model with unloading ($J_2$ flow theory) both with the same uniaxial response). It is found that plasticity plays an important role as we approach $\tau_m$, since elastic unloading leads to concentration of deformation in a few narrow bands that link-up to cover the entire domain.

The above approach is useful for the stability analysis of different types of structures under rapid strain rates. As one such example we cite the work by [19] on the stability of a pressurized thin ring at high rates, where it is shown that for small values of the applied loading rate, the structure fails through a global (ellipsoidal) mode, while for large values of the applied loading rate the structure fails by a localized mode of deformation, as also found experimentally by [15].

## Appendix A: Constitutive Laws Adopted and Their Plane Stress Incremental Moduli

Although the expressions for the 2D plane stress incremental moduli are stated in [29], their derivation from 3D considerations is interesting and hence, for the sake of completeness of the presentation, the details of the corresponding derivations are given in this Appendix.

The analysis presented in Sect. 2 is general; any rate-independent constitutive law[16] which can be put in the form of (2.5), can be accommodated. Results presented here correspond to the three such models: a *hyperelastic deformation theory* model of plasticity, the $J_2$ *deformation theory* model of [24] and a finite strain generalization of the $J_2$ *flow theory*. All models are fitted to the same power law uniaxial stress-strain curve and thus share the same principal solution. For further details on this construction, the interested reader is referred to [26]. For the small perturbations considered here, deviations from proportional loading are initially small and no unloading occurs in the perturbed plate until well after $\tau_m$ (the time corresponding to the loss of ellipticity onset in the unperturbed – uniform strain – solution), thus justifying their use for analyzing the plate's stability.

Assuming material incompressibility, the [24] $J_2$ deformation and the $J_2$ flow theory models that can be put in the following 3D rate form

$$\overset{\triangledown}{\boldsymbol{\sigma}} = \boldsymbol{C} : \boldsymbol{D} - \dot{p}\boldsymbol{I}, \tag{A.1}$$

[16] Localization of deformation requires that the constitutive law looses ellipticity at some strain level.

where $\overset{\triangledown}{(\ )}$ denotes the *Jaumann rate* of the Cauchy stress tensor ($\overset{\triangledown}{\boldsymbol{\sigma}} = \dot{\boldsymbol{\sigma}} - \boldsymbol{\Omega}\cdot\boldsymbol{\sigma} + \boldsymbol{\sigma}\cdot\boldsymbol{\Omega}$ with $\boldsymbol{\Omega}$ the *spin* tensor), $\boldsymbol{D}$ is the *strain rate* tensor and $\dot{p}$ the hydrostatic pressure rate.

For the case of finite strains, the above 3D current configuration relation can be transformed into its reference configuration counterpart

$$\dot{S}_{ij} = L_{ijkl}\dot{E}_{kl} - \dot{p}C^{-1}_{ij}; \quad E_{ij} = \frac{1}{2}\big(C_{ij} - \delta_{ij}\big), \tag{A.2}$$

where $\boldsymbol{S}$ is the *second Piola-Kirchhoff stress*, $\boldsymbol{E}$ its work-conjugate *Green-Lagrange strain* and the reference configuration components of the *incremental moduli tensor* $\boldsymbol{L}$ are

$$\begin{aligned} L_{ijkl} \equiv \frac{2}{3}E^*\Big[\frac{1}{2}\big(C^{-1}_{ik}C^{-1}_{jl} + C^{-1}_{il}C^{-1}_{jk}\big) - \frac{3}{2}\Big(1 - \frac{E_t}{E^*}\Big)\frac{S'_{ij}S'_{kl}}{\sigma_e^2}\Big] \\ - \frac{1}{2}\Big[C^{-1}_{ik}S_{jl} + C^{-1}_{jk}S_{il} + C^{-1}_{il}S_{jk} + C^{-1}_{jl}S_{ik}\Big], \end{aligned} \tag{A.3}$$

where $\boldsymbol{S}'$ is the deviatoric part of the stress tensor $\boldsymbol{S}$ and $\sigma_e$ the *von Mises equivalent stress*, namely

$$S'_{ij} = S_{ij} - \frac{1}{3}C^{-1}_{ij}C_{kl}S_{kl}, \quad \sigma_e^2 = \frac{3}{2}C_{ik}C_{jl}S'_{ij}S'_{kl}. \tag{A.4}$$

In the above expressions $E^* = E$ for the $J_2$ flow theory while for the $J_2$ deformation theory of [24] $E^* = E_s \equiv \sigma_e/\epsilon_e$ is the *secant modulus* of the uniaxial stress-strain curve. In both models $E_t$ is the *tangent modulus* of the uniaxial stress-strain curve $E_t \equiv \mathrm{d}\sigma_e/\mathrm{d}\epsilon_e$. For the $J_2$ hyperelastic model the general expression for $E^*$ is more complicated and will be given below for the special case of the biaxially stretched membrane.

The principal axes expressions in three dimensions for the (von Mises) equivalent stress $\sigma_e$ and the *equivalent strain* $\epsilon_e$, required for the calculation of $E_s$ and $E_t$ are

$$\sigma_e = \big(\sigma_1^2+\sigma_2^2+\sigma_3^2-\sigma_1\sigma_2-\sigma_2\sigma_3-\sigma_3\sigma_1\big)^{1/2}, \quad \epsilon_e = \frac{2}{3}\big(\epsilon_1^2+\epsilon_2^2+\epsilon_3^2-\epsilon_1\epsilon_2-\epsilon_2\epsilon_3-\epsilon_3\epsilon_1\big)^{1/2}. \tag{A.5}$$

Due to plane stress loading conditions

$$\dot{S}_{3i} = 0, \quad \dot{E}_{\alpha 3} = 0, \quad \dot{E}_{33} = -C_{33}C^{-1}_{\gamma\delta}\dot{E}_{\gamma\delta}, \tag{A.6}$$

which substituted in (A.2) give the following relation between $\dot{S}_{\alpha\beta}$ and its work conjugate $\dot{E}_{\alpha\beta}$

$$\dot{S}_{\alpha\beta} = \mathcal{M}_{\alpha\beta\gamma\delta}\dot{E}_{\gamma\delta}; \quad \mathcal{M}_{\alpha\beta\gamma\delta} = L_{\alpha\beta\gamma\delta} - C_{33}\big(L_{\alpha\beta 33}C^{-1}_{\gamma\delta} + C^{-1}_{\alpha\beta}L_{33\gamma\delta}\big) + C^{-1}_{\alpha\beta}C^{-1}_{\gamma\delta}C^2_{33}L_{3333}. \tag{A.7}$$

The above result, combined with (A.3) gives the following expression for $M_{\alpha\beta\gamma\delta}$

$$\begin{aligned} \mathcal{M}_{\alpha\beta\gamma\delta} = \frac{2}{3}E^*\Big[\frac{1}{2}\big(C^{-1}_{\alpha\gamma}C^{-1}_{\beta\delta} + C^{-1}_{\alpha\delta}C^{-1}_{\beta\gamma}\big) + C^{-1}_{\alpha\beta}C^{-1}_{\gamma\delta} - \frac{3}{2}\Big(1 - \frac{E_t}{E^*}\Big)\frac{S'_{\alpha\beta}S'_{\gamma\delta}}{\sigma_e^2}\Big] \\ - \frac{1}{2}\Big[C^{-1}_{\alpha\gamma}S_{\beta\delta} + C^{-1}_{\beta\gamma}S_{\alpha\delta} + C^{-1}_{\alpha\delta}S_{\beta\gamma} + C^{-1}_{\beta\delta}S_{\alpha\gamma}\Big]. \end{aligned} \tag{A.8}$$

Recalling the relations between $\boldsymbol{S}$ & $\boldsymbol{N}$ and $\boldsymbol{E}$ & $\boldsymbol{F}$, the plane stress incremental moduli $\boldsymbol{\mathcal{L}}$ in (2.5) are found to be

$$\mathcal{L}_{\alpha\beta\gamma\delta} = \mathcal{M}_{\epsilon\beta\zeta\delta}F_{\alpha\epsilon}F_{\gamma\zeta} + S_{\delta\beta}\delta_{\alpha\gamma}. \tag{A.9}$$

For the case of biaxial loading of interest here $F_{\alpha\beta} = \text{diag}\,(\lambda_\gamma)$ and thus

$$C_{11} = \lambda_1^2, \quad C_{22} = \lambda_2^2, \quad C_{12} = 0; \quad S_{11} = \sigma_1/\lambda_1^2, \quad S_{22} = \sigma_2/\lambda_2^2, \quad S_{12} = 0, \tag{A.10}$$

which upon substitution into (A.8), (A.9) gives the incremental moduli expressions in (A.16), (A.17) for $J_2$ flow and $J_2$ deformation theories.

Calculations of the moduli for the hyperelastic model use (A.9), (A.10) and $\boldsymbol{\mathcal{M}}$ is derived from the strain energy potential $W$

$$\mathcal{M}_{\alpha\beta\gamma\delta} = \frac{\partial^2 W}{\partial E_{\alpha\beta}\partial E_{\gamma\delta}} = 4\frac{\partial^2 W}{\partial C_{\alpha\beta}\partial C_{\gamma\delta}}, \tag{A.11}$$

obtained by successive application of chain rule of differentiation using $W(\epsilon_e)$ where the equivalent strain $\epsilon_e = \epsilon_e(I_1, I_2)$ is expressed in terms of the invariants of $\boldsymbol{C}$, which in turn depend on the principal stretch ratios $\lambda_\alpha$ through

$$I_1 = \text{tr}\,\boldsymbol{C} = \lambda_1^2 + \lambda_2^2, \quad I_2 = \det \boldsymbol{C} = \big(\lambda_1\lambda_2\big)^2. \tag{A.12}$$

The 3D strain energy density $W$ used here is a function of the equivalent strain $\epsilon_e$; the isotropic model is fitted to a piecewise power law uniaxial stress-strain curve[17] resulting in the following expressions for $W$

$$\frac{\sigma_e}{\sigma_y} = \Big(\frac{\epsilon_e}{\epsilon_y}\Big)^m; \quad W = E\big(\epsilon_y\big)^2\Big[\frac{1}{1+m}\Big(\frac{\epsilon_e}{\epsilon_y}\Big)^{m+1} + \frac{1}{2}\Big(\frac{m-1}{m+1}\Big)\Big], \quad \begin{cases} m = 1 \text{ for } \epsilon_e \le \epsilon_y, \\ m = n \text{ for } \epsilon_e > \epsilon_y, \end{cases} \tag{A.13}$$

where the equivalent strain $\epsilon_e$ is given in terms of the principal logarithmic strain components $\epsilon_\alpha$ by (A.5). Accounting for the incompressibility constraint $\epsilon_1 + \epsilon_2 + \epsilon_3 = 0$ (A.5) one obtains

$$\sigma_e = \big(\sigma_1^2 + \sigma_2^2 - \sigma_1\sigma_2\big)^{1/2}, \quad \epsilon_e = \frac{2}{\sqrt{3}}\Big[\epsilon_1^2 + \epsilon_2^2 + \epsilon_1\epsilon_2\Big]^{1/2}, \tag{A.14}$$

where the equivalent stress $\sigma_e$ expression accounts for the plane stress condition $\sigma_3 = 0$ and the equivalent strain accounts for incompressibility $\epsilon_1 + \epsilon_2 + \epsilon_3 = 0$. Since the principal solution is biaxial straining, the principal Cauchy stresses $\sigma_\alpha$ are related to their work-conjugate the principal logarithmic strains $\epsilon_\alpha$ by:

$$\sigma_\alpha = \frac{\partial W}{\partial \epsilon_\alpha}, \; \sigma_1 = \frac{2}{3}E_s\big(2\epsilon_1 + \epsilon_2\big), \; \sigma_2 = \frac{2}{3}E_s\big(\epsilon_1 + 2\epsilon_2\big); \quad \epsilon_\alpha = \ln\lambda_\alpha, \tag{A.15}$$

where the secant $E_s$ and tangent $E_t$ moduli of the uniaxial stress-strain curve that appear in (A.3).

After some lengthy algebra we end in the following expressions for the non-zero components of the plane stress moduli in (2.6), given below in two groups; the *normal moduli*

[17] Note: for a uniaxial stress state $\epsilon_2 = -\epsilon_1/2$ and $\epsilon_e = \epsilon$; Moreover $\epsilon_y$ and $\sigma_y = E\epsilon_y$ are the yield strain and stress respectively in a uniaxial loading path.

components are:

$$\begin{aligned}
\mathcal{L}_{1111} &= \frac{1}{\lambda_1^2}\Big[\frac{4}{3}E^* + \big(E_t - E^*\big)\Big(\frac{\sigma_1}{\sigma_e}\Big)^2 - \sigma_1\Big],\\
\mathcal{L}_{1122} = \mathcal{L}_{2211} &= \frac{1}{\lambda_1\lambda_2}\Big[\frac{2}{3}E^* + \big(E_t - E^*\big)\frac{\sigma_1\sigma_2}{\sigma_e^2}\Big],\\
\mathcal{L}_{2222} &= \frac{1}{\lambda_2^2}\Big[\frac{4}{3}E^* + \big(E_t - E^*\big)\Big(\frac{\sigma_2}{\sigma_e}\Big)^2 - \sigma_2\Big],
\end{aligned} \tag{A.16}$$

and the *shear moduli* components are given by:

$$\begin{aligned}
\mathcal{L}_{1212} &= \frac{1}{\lambda_2^2}\Big[\frac{E^*}{3} + \frac{\sigma_2 - \sigma_1}{2}\Big],\\
\mathcal{L}_{2121} &= \frac{1}{\lambda_1^2}\Big[\frac{E^*}{3} + \frac{\sigma_1 - \sigma_2}{2}\Big],\\
\mathcal{L}_{1221} = \mathcal{L}_{2112} &= \frac{1}{\lambda_1\lambda_2}\Big[\frac{E^*}{3} - \frac{\sigma_1 + \sigma_2}{2}\Big],
\end{aligned} \tag{A.17}$$

where for the $J_2$ flow theory $E^* = E$, the $J_2$ deformation theory $E^* = E_s$ and the hyperelastic model $E^* = E_s[(\lambda_1^2 + \lambda_2^2)/(\lambda_1^2 - \lambda_2^2)](\ln\lambda_1 - \ln\lambda_2)$ where these quantities were defined immediately after (A.4). Derivation details for the hyperelastic model can be found in [26]. The principal stresses $\sigma_\alpha$ for all three models are identical and given by (A.15).

In the above expressions the material energy density $W$ is the 3D version. We use here in Appendix A the same symbol as for its 2D counterpart in Sect. 2 to avoid extra symbols. In the same spirit, the dimensionless version of the stresses $\sigma_\alpha$ and moduli $\mathcal{L}_{\alpha\beta\gamma\delta}$ in (A.15), (A.16) and (A.17), are found by taking in all the above expressions the initial Young modulus to be $E = 1$.

## Appendix B: Influence Discs as Functions of Constitutive Law and Load Orientation

The minimum and maximum influence disc sizes $\delta_-$, defined in (2.12), and $\delta_+$,defined in (2.13), at the onset of loss of ellipticity $\tau_m$, have been presented in [29]. However, for the sake of completeness of the presentation and also in view of a different definition of $\delta_+$ adopted in this paper, these results are presented again here in Fig. 13 with the disc sizes given as functions of the load orientation angle $\psi$ for the three different constitutive models considered in Appendix A and for two different power-law hardening exponents, $n = 0.22$ (typical of Al alloys, plotted in solid lines) and $n = 0.40$ (typical of steel alloys, plotted in dotted lines). Curves in the $\psi < 0$ range are terminated at $\psi = \tan^{-1}(-0.5)$ below which one stress becomes compressive. Moreover, $J_2$ flow theory curves are only plotted for $\psi \le 0$, in view of their well-known – see [24] – unrealistic predictions for $\psi > 0$.

As expected, for a given material and load orientation $\psi$, both $\delta_-$ and $\delta_+$ are increasing functions of the hardening exponent $n$. For the lower hardening exponent $n = 0.22$, there is practically no difference for either the minimum or maximum influence disc sizes, $\delta_-$ and $\delta_-$ respectively, between the $J_2$ deformation and hyperelastic theory models over the entire range of load orientations considered. For the higher hardening exponent $n = 0.4$, the $\delta_-$ predictions of the $J_2$ deformation and hyperelastic theory models are practically the

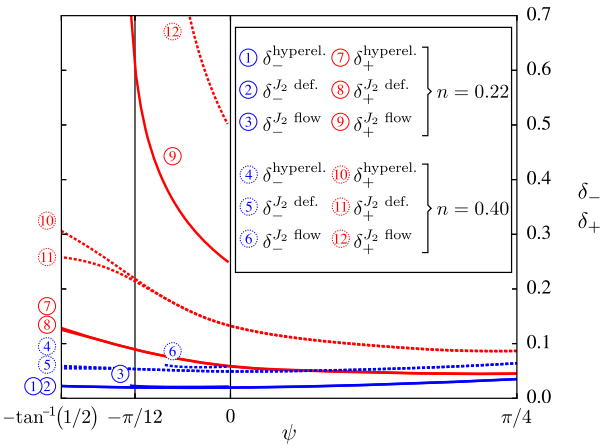


**Fig. 13** Minimum $\delta_-$ and maximum $\delta_+$ influence disc sizes at the onset of loss of ellipticity $\tau_m$, as functions of the load orientation angle $\psi$ for the three different constitutive models considered: hyperelastic, $J_2$-deformation theory and $J_2$-flow theory, all sharing the same uniaxial stress-strain law with $\epsilon_y = 0.002$ and $n = 0.22$ (solid line) and $n = 0.40$ (dotted line)

same over the entire range of loading angles, while the maximum influence disc size $\delta_+$ predictions for these two constitutive models start diverging at about $\psi < -\pi/12$.

Setting aside the fact that $\delta_-$ and $\delta_+$ exist for a significantly smaller range of load orientations for the much stiffer $J_2$ flow theory, one can observe that for $n = 0.22$ there is no noticeable increase in the $J_2$ flow theory value of $\delta_-$ compared to its hyperelastic and deformation theory counterparts, but there is a large increase in the corresponding value of $\delta_+$, as compared to the other two constitutive models with the same uniaxial curve. The same trend holds true for $n = 0.40$, but the differences between constitutive models, especially for $\delta_+$, are considerably larger. Moreover, the $J_2$ flow theory gives unrealistically high values for $\delta_+$, save for a small range near $\psi = 0$.

The small difference of the minimum $\delta_-$ and maximum $\delta_+$ influence disc sizes predicted by the hyperelastic and $J_2$ deformation theory constitutive models is the reason for using the simpler to implement hyperelastic model in most of our numerical calculations.

## Appendix C: Critical ($\tau_m$) and Stability Limit ($\tau_L$) Dimensionless Times

Having established the incremental moduli tensor $\mathcal{L}$ in Appendix A for the constitutive laws adopted in this work, we calculate next the dimensionless critical time $\tau_m$ for the onset of loss of ellipticity, the corresponding localization angle $\phi_m$ introduced in (2.11) and the dimensionless Lyapunov stability time $\tau_L$ in order to establish the range of validity of the plate's linearized stability, as presented in Sect. 2.2.

From the definition of $\mathbf{A}$ in (2.7) we have

$$\mathbf{A}(\tau,\phi) = \begin{bmatrix} \mathcal{L}_{1111}(\tau)(n_1)^2 + \mathcal{L}_{1212}(\tau)(n_2)^2 & (\mathcal{L}_{1122}(\tau) + \mathcal{L}_{1221}(\tau))(n_1 n_2) \\ (\mathcal{L}_{2211}(\tau) + \mathcal{L}_{2112}(\tau))(n_1 n_2) & \mathcal{L}_{2121}(\tau)(n_1)^2 + \mathcal{L}_{2222}(\tau)(n_2)^2 \end{bmatrix};$$

$$n_1 = \cos(\phi),\ n_2 = \sin(\phi), \tag{C.1}$$

and from the definitions in (2.11) and (2.10), $\tau_m$ is the lowest positive $\tau$ root of the characteristic equation of $\boldsymbol{A}(\tau,\phi), \forall \phi \in [0, \pi/2]$

$$\mathcal{L}_{1111}(\tau)\mathcal{L}_{2121}(\tau)(n_1)^4 + [\mathcal{L}_{1111}(\tau)\mathcal{L}_{2222}(\tau) + \mathcal{L}_{1212}(\tau)\mathcal{L}_{2121}(\tau) - (\mathcal{L}_{1122}(\tau)\mathcal{L}_{1221}(\tau))^2](n_1 n_2)^2 + \mathcal{L}_{1212}(\tau)\mathcal{L}_{2222}(\tau)(n_2)^4. \tag{C.2}$$

For the loading angles $\psi$ considered in Sect. 3, we find

$$\begin{aligned}
\psi = -\frac{\pi}{12} : \quad & [\mathcal{L}_{1111}(\tau_m)\mathcal{L}_{2222}(\tau_m)]^{1/2} + [\mathcal{L}_{1212}(\tau_m)\mathcal{L}_{2121}(\tau_m)]^{1/2} \\
& - [\mathcal{L}_{1122}(\tau_m) + \mathcal{L}_{1221}(\tau_m)] = 0, \\
\psi = 0 \quad : \quad & \mathcal{L}_{1111}(\tau_m) = 0 \Longrightarrow \tau_m = \exp(n) - 1, \\
\psi = \frac{\pi}{4} \quad : \quad & \mathcal{L}_{1111}(\tau_m) = 0 \Longrightarrow \tau_m = \left[\exp((1+3n)/6) - 1\right]\sqrt{2},
\end{aligned} \tag{C.3}$$

where the corresponding angles in the interval $[0, \pi/2]$ are

$$\begin{aligned}
& \psi = -\frac{\pi}{12} \ : \ \phi_m = \tan^{-1}\left[\frac{\mathcal{L}_{1111}(\tau_m)\mathcal{L}_{2121}(\tau_m)}{\mathcal{L}_{1212}(\tau_m)\mathcal{L}_{2222}(\tau_m)}\right]^{1/4}, \quad \psi = 0 \ : \ \phi_m = 0, \\
& \psi = \frac{\pi}{4} \ : \ \forall \phi_m \in \left[0, \frac{\pi}{2}\right].
\end{aligned} \tag{C.4}$$

Notice that for loading angles $\psi = 0, \pi/4$, the critical time is independent of the particular version of the model used (hyperelastic, $J_2$ deformation or $J_2$ flow theory) and depends solely on the exponent $n$[18] of the power law-type uniaxial stress-strain curve in (A.14).

The Lyapunov (linearized) stability of the system, as discussed in Sect. 2.2, is guaranteed by the positive definiteness of $\boldsymbol{A}(\tau, \phi)$ and $-\dot{\boldsymbol{A}}(\tau, \phi)$. By construction $\boldsymbol{A}(\tau, \phi)$ is positive definite for $\forall \tau \in [0, \tau_m)$, $\forall \phi \in [0, \pi/2]$. Finding the value of $\tau_L \leq \tau_m$ that guarantees the positive definiteness of $-\dot{\boldsymbol{A}}(\tau, \phi)$ for $\forall \tau \in [0, \tau_L)$, $\forall \phi \in [0, \pi/2]$ is based on numerical calculations using a symbolic manipulator.

For the cases investigated in Sect. 3 the following values are found for the dimensionless critical time $\tau_m$ and the corresponding linearized (Lyapunov) stability time $\tau_L$

$$\text{hyperelastic ; } n = 0.22 \quad \begin{cases}
\psi = \tan^{-1}\left(-\frac{1}{2}\right), & \tau_m = 0.508, \quad \tau_L = 0.38 \\
\psi = -\frac{\pi}{12}, & \tau_m = 0.352, \quad \tau_L = \tau_m \\
\psi = 0, & \tau_m = 0.246, \quad \tau_L = \tau_m \\
\psi = \frac{\pi}{4}, & \tau_m = 0.451, \quad \tau_L = \tau_m
\end{cases}$$

$$n = 0.40 \quad \begin{cases}
\psi = \tan^{-1}\left(-\frac{1}{2}\right), & \tau_m = 0.900, \quad \tau_L = 0.33 \\
\psi = -\frac{\pi}{12}, & \tau_m = 0.715, \quad \tau_L = 0.475 \\
\psi = 0, & \tau_m = 0.492, \quad \tau_L = \tau_m \\
\psi = \frac{\pi}{4}, & \tau_m = 0.626, \quad \tau_L = \tau_m
\end{cases}$$

$$J_2 \text{ deformation ; } n = 0.22 \quad \begin{cases}
\psi = \tan^{-1}\left(-\frac{1}{2}\right), & \tau_m = 0.482, \quad \tau_L = 0.44 \\
\psi = -\frac{\pi}{12}, & \tau_m = 0.351, \quad \tau_L = \tau_m \\
\psi = 0, & \tau_m = 0.246, \quad \tau_L = \tau_m \\
\psi = \frac{\pi}{4}, & \tau_m = 0.451, \quad \tau_L = \tau_m
\end{cases}$$

[18] For the value of $\epsilon_y = 0.002$ used in the calculations of Sect. 3, the equivalent strain verifies $\epsilon_e(\tau_m) > \epsilon_y$.

$$
\begin{array}{ll}
n=0.40 & \begin{cases}
\psi=\tan^{-1}\left(-\dfrac{1}{2}\right), & \tau_m=0.723, \quad \tau_L=0.38 \\
\psi=-\dfrac{\pi}{12}, & \tau_m=0.689, \quad \tau_L=0.620 \\
\psi=0, & \tau_m=0.492, \quad \tau_L=\tau_m \\
\psi=\dfrac{\pi}{4}, & \tau_m=0.626, \quad \tau_L=\tau_m
\end{cases} \\
J_2 \text{ flow } ; \, n=0.22 & \begin{cases}
\psi=\tan^{-1}\left(-\dfrac{1}{2}\right), & \tau_m=0.756, \quad \tau_L=0 \\
\psi=-\dfrac{\pi}{12}, & \tau_m=0.405, \quad \tau_L=0 \\
\psi=0, & \tau_m=0.246, \quad \tau_L=0
\end{cases} \\
n=0.40 & \begin{cases}
\psi=\tan^{-1}\left(-\dfrac{1}{2}\right), & \tau_m=0.924, \quad \tau_L=0 \\
\psi=-\dfrac{\pi}{12}, & \tau_m=1.131, \quad \tau_L=0 \\
\psi=0, & \tau_m=0.492, \quad \tau_L=0
\end{cases}
\end{array}
\tag{C.5}
$$

It is worth noticing in (C.5) that – for the same hardening exponent $n$ – the results for the hyperelastic and $J_2$ deformation theory models are either very close (or coincident for $\psi = 0, \pi/4$), while the much stiffer $J_2$ flow theory is not linearly stable since $-\dot{\boldsymbol{A}}(\tau, \phi)$ looses positive definiteness for certain values of $\phi$ at all dimensionless times $\tau$ (and hence $\tau_L = 0$).

**Acknowledgements** This paper is dedicated to the memory Prof. J. Ericksen. The work was initiated in part by grants from École Polytechnique and the CNRS (Centre National de Recherche Scientifique) during the AY 2011-2012, during the second author's sabbatical leave as a Distinguished Visiting Professor of the École Polytechnique, in residence at the École's Solid Mechanics Laboratory (LMS). This work continued during several subsequent visits, made possible through the generosity of LMS and the École Polytechnique and was finalized during the June 2022 visit of Prof. R. S. Elliott, also supported by the LMS. We also acknowledge some very helpful discussions on dynamic systems stability with applications in fluid mechanics with Prof. L. Guin from École Polytechnique.

**Author contributions** G.W. performed the numerical simulations and prepared the figures. N.T., R.E., and K.R. wrote the main manuscript text and contributed to the problem formulation and results analysis. All authors reviewed the manuscript.

## Declarations

**Competing interests** The authors declare no competing interests.

## References

1. Abeyaratne, R., Triantafyllidis, N.: The emergence of shear bands in plane strain. Int. J. Solids Struct. **17**, 1113–1134 (1981)
2. Bernstein, D.S.: Matrix Mathematics; Theory, Facts, and Formulas. Princeton University Press, Princeton (2009)
3. Brush, D., Almroth, B.: Buckling of Bars, Plates, and Shells. McGraw-Hill, New York (1975)
4. Budiansky, B., Hutchinson, J.: Dynamic buckling of imperfection sensitive structures. Proc. XI Int. Cong. Appl. Mech., pp. 636–651. (1964)
5. Clifton, R.J., Duffy, J., Hartley, K.A., Shawki, T.G.: On critical conditions for shear bar formation at high strain rates. Scr. Metall. **18**, 443–448 (1984)
6. Dequiedt, J.L.: Statistics of dynamic fragmentation for a necking instability. Int. J. Solids Struct. **75**, 32–44 (2015)

7. El Mai, S., Mercier, S., Petit, J., Molinari, A.: An extension of the linear stability analysis for the prediction of multiple necking during dynamic extension of round bar. Int. J. Solids Struct. **51**, 3491–3507 (2014)
8. Fressengeas, C., Molinari, A.: Inertia and thermal effects on the localization of plastic flow. Acta Metall. Mater. **33**, 387–396 (1985)
9. Fressengeas, C., Molinari, A.: Fragmentation of rapidly stretching sheets. Eur. J. Mech. A, Solids **13**(2), 251 (1994)
10. Guduru, P., Freund, L.: The dynamics of multiple neck formation and fragmentation in high rate extension of ductile materials. Int. J. Solids Struct. **39**, 5615–5632 (2002)
11. Guduru, P.R., Bharathi, M.S., Freund, L.: The influence of a surface coating on the high-rate fragmentation of a ductile material. Int. J. Fract. **137**(1–4), 89–108 (2006)
12. Jouve, D.: Analytic study of the onset of plastic necking instabilities during biaxial tension tests on metallic plates. Eur. J. Mech. A, Solids **50**, 59–69 (2015)
13. Koiter, W.T.: The Stability of Elastic Equilibrium (in Dutch) English Translation: Technical Report No. AFFDL-TR-70-25, sponsored by Lockheed Missiles and Space Co., February 1970 Ph.D. thesis. Technische Hooge School Delft (1945)
14. Koning, C., Taub, J.: Impact buckling of thin bars in the elastic range hinged at both ends. Luftfahrt-Forsch. **10**, 55–64 (1933)
15. Mainy, A.: Dynamic buckling of thin metallic rings under external pressure. Master's thesis, University of Texas (2012)
16. Mercier, S., Granier, N., Molinari, A., Liorca, F., Buy, F.: Multiple necking during the dynamic expansion of hemispherical metallic shells, from experiments to modelling. J. Mech. Phys. Solids **58**, 955–982 (2010)
17. Mercier, S., Molinari, A.: Predictions of bifurcations and instabilities during dynamic extensions. Int. J. Solids Struct. **40**, 1995–2016 (2003)
18. Molnár, G., Gravouil, A., Seghir, R., Réthoré, J.: An open-source abaqus implementation of the phase-field method to study the effect of plasticity on the instantaneous fracture toughness in dynamic crack propagation. Comput. Methods Appl. Mech. Eng. **364**, 11304 (2020)
19. Putelat, T., Triantafyllidis, N.: Dynamic stability of externally pressurized elastic rings subjected to high rates of loading. Int. J. Solids Struct. **51**, 1–12 (2014)
20. Ravi-Chandar, K., Triantafyllidis, N.: Dynamic stability of a bar under high loading rate: response to local perturbations. Int. J. Solids Struct. **58**, 301–308 (2015)
21. Rodrigues-Martinez, J.A., Vadillo, G., Fernandez-Saez, J., Molinari, A.: Identification of the critical wavelength responsible for the fragmentation of ductile rings expanding at very high strain rates. J. Mech. Phys. Solids **61**, 1357–1376 (2013)
22. Rodríguez-Martínez, J.A., Molinari, A., Zaera, R., Fernández-Sáez, J.: The critical neck spacing in ductile plates subjected to dynamic biaxial loading: on the interplay between loading path and inertia effects. Int. J. Solids Struct. **108**, 74–84 (2017)
23. Shenoy, V., Freund, L.: Necking bifurcations during high strain rate extension. J. Mech. Phys. Solids **47**, 2209–2233 (1999)
24. Stören, S., Rice, J.R.: Localized necking in thin sheets. J. Mech. Phys. Solids **23**, 421–441 (1975)
25. Trefethen, L.N., Trefethen, A.E., Reddy, S.C., Driscoll, T.A.: Hydrodynamic stability without eigenvalues. Science **261**, 578–584 (1993)
26. Triantafyllidis, N.: Bifurcation phenomena in pure bending. J. Mech. Phys. Solids **28**, 221–245 (1980)
27. Vaz-Romero, A., Mercier, S., Rodrigues-Martinez, J.A., Molinari, A.: A comparative study of the dynamic fragmentation of non-linear elastic and elasto-plastic rings: the roles of stored elastic energy and plastic dissipation. Mech. Mater. **132**, 134–148 (2019)
28. Vaz-Romero, A., Rodríguez-Martínez, J.A., Mercier, S., Molinari, A.: Multiple necking pattern in non-linear elastic bars subjected to dynamic stretching: the role of defects and inertia. Int. J. Solids Struct. **125**, 232–243 (2017)
29. Wen, G., Triantafyllidis, N.: Dynamic stability of biaxially strained thin sheets under high strain-rates: response to local perturbations. Int. J. Fract. **200**, 99–113 (2016)
30. Xue, Z., Vaziri, A., Hutchinson, J.: Material aspects of dynamic neck retardation. J. Mech. Phys. Solids **56**, 93–113 (2008)
31. Zaera, R.: Collective behaviour and spacing of necks in ductile plates subjected to dynamic biaxial loading. J. Mech. Phys. Solids **85**, 245–269 (2015)
32. Zhang, H., Ravi-Chandar, K.: On the dynamics of necking and fragmentation – I. Real-time and post-mortem observations in Al 6061-O. Int. J. Fract. **142**, 183–217 (2006)
33. Zhang, H., Ravi-Chandar, K.: On the dynamics of necking and fragmentation – II. Effect of material properties, geometrical constraints and absolute size. Int. J. Fract. **150**, 3–36 (2008)

34. Zhang, H., Ravi-Chandar, K.: On the dynamics of necking and fragmentation – IV. Expansion of al 6061-o tubes. Int. J. Fract. **163**, 41–65 (2010)
35. Zhou, F., Molinari, J., Ramesh, K.T.: An elastic–visco-plastic analysis of ductile expanding ring. Int. J. Impact Eng. **33**, 880–891 (2006)



## Authors and Affiliations

**G. Wen[1] · K. Ravi-Chandar[2] · R.S. Elliott[3] · N. Triantafyllidis[1,4,5]**

✉ R.S. Elliott
relliott@umn.edu

1 LMS, École Polytechnique, CNRS UMR7649, Institut Polytechnique de Paris, Palaiseau 91128, France

2 Aerospace Engineering & Engineering Mechanics Department, The University of Texas, Austin TX 78712, USA

3 Aerospace Engineering & Mechanics, University of Minnesota, Minneapolis MN 55455, USA

4 Département de Mécanique, École Polytechnique, Palaiseau 91128, France

5 Aerospace Engineering Dept. & Mechanical Engineering Dept. (emeritus), The University of Michigan, Ann Arbor MI 48105, USA